THE JOURNAL OF PHYSICAL CHEMISTRY B
A JOURNAL OF THE AMERICAN CHEMICAL SOCIETY

pubs.acs.org/JPCB

Article

Ultrafast Dynamics and Liquid Structure in Mesoporous Silica: Propagation of Surface Effects in a Polar Aprotic Solvent

Samantha T. Hung, Steven A. Yamada, Weizhong Zheng,* and Michael D. Fayer*

Cite This: *J. Phys. Chem. B* 2021, 125, 10018–10034

Read Online

ACCESS | Metrics & More | Article Recommendations | Supporting Information

ABSTRACT: Enhancement of processes ranging from gas sorption to ion conduction in a liquid can be substantial upon nanoconfinement. Here, the dynamics of a polar aprotic solvent, 1-methylimidazole (MeIm), in mesoporous silica (2.8, 5.4, and 8.3 nm pore diameters) were examined using femtosecond infrared vibrational spectroscopy and molecular dynamics simulations of a dilute probe, the selenocyanate ($SeCN^-$) anion. The long vibrational lifetime and sensitivity of the CN stretch enabled a comprehensive investigation of the relatively slow time scales and subnanometer distance dependences of the confined dynamics. Because MeIm does not readily donate hydrogen bonds, its interactions in the hydrophilic silanol pores differ more from the bulk than those of water confined in the same mesopores, resulting in greater structural order and more dramatic slowing of dynamics. The extent of surface effects was quantified by modified two-state models used to fit three spatially averaged experimental observables: vibrational lifetime, orientational relaxation, and spectral diffusion. The length scales and the models (smoothed step, exponential decay, and simple step) describing the transitions between the distinctive shell behavior at the surface and the bulk-like behavior at the pore interior were compared to those of water. The highly nonuniform distributions of the $SeCN^-$ probe and antiparallel layering of MeIm revealed by the simulations guided the interpretation of the results and development of the analytical models. The results illustrate the importance of electrostatic effects and H-bonding interactions in the behavior of confined liquids.

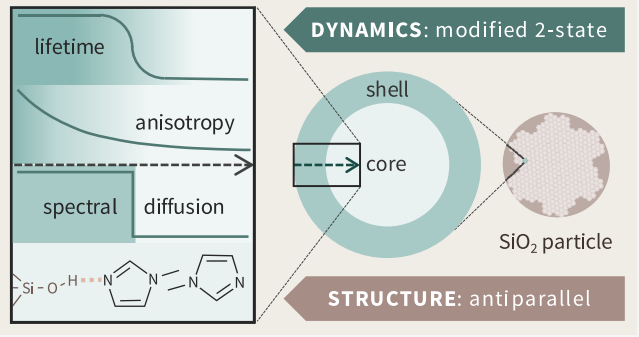

1. INTRODUCTION

Nanoconfined liquid dynamics are important in a wide range of naturally occurring and technologically important systems. In particular, liquids in mesoporous silicas (pore diameter 2–50 nm) have broad importance, e.g., hybrid electrolytes,[1,2] heterogeneous catalysis,[3,4] and carbon capture.[5] Due to the ubiquity and importance of aqueous systems, the structure and dynamics of confined water have been studied extensively.[6−22] Simulation[23−29] and experimental[30−33] (neutron scattering, optical Kerr effect, and NMR) confinement studies have been conducted for a few simple organic liquids like acetonitrile and benzene. In general, dynamics slow with increasing confinement, but the rate of formation of an imidazolium-based ionic liquid (IL) by chemical reaction from 1-methylimidazole increased upon confinement in mesoporous silica.[4] The ionic conductivity of another imidazolium-based IL increased by nearly 1000-fold when polymerized *in situ* in mesoporous silica.[1] A molecular understanding of how nanoconfinement results in distinct properties for different types of liquids can shed light on disparate effects resulting from confinement and inform the rational design of novel processes and materials.

The highly uniform but size-tunable, cylindrical pores of MCM41 and SBA15 type silicas[34−36] enable quantitative studies of ultrafast dynamics and underlying intermolecular interactions under well-defined levels of nanoscale confinement. Their large surface areas yield high active site densities, which are often responsible for the desired confinement effects, from stabilizing transition states in reactions[4] to inducing favorable orientational preferences.[1] Predicting optimal dimensions of confinement thus necessitates an understanding of the dependences of different, and potentially counteracting, liquid properties on the distance from the silica surface.

The dynamics of a polar aprotic solvent, 1-methylimidazole (MeIm, Figure 1), confined in a series of mesoporous silica pore sizes were measured by infrared (IR) polarization selective pump-probe (PSPP) and two-dimensional IR (2D IR) experiments on the nitrile (CN) stretching mode of a selenocyanate ($SeCN^-$) vibrational probe. The long vibrational lifetime of the small $SeCN^-$ probe (>100 ps in MeIm) and its sensitivity to local solvent interactions and structure[37−39]

Received: May 31, 2021
Revised: August 6, 2021
Published: August 27, 2021

https://doi.org/10.1021/acs.jpcb.1c04798
J. Phys. Chem. B 2021, 125, 10018–10034

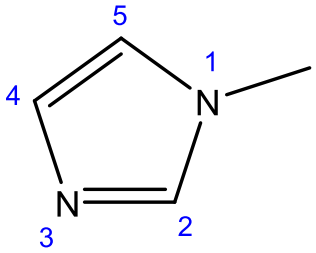

1-Methylimidazole (MeIm)

Figure 1. Molecular structure of 1-methylimidazole (MeIm) with numbering scheme.

enable the measurement of the long time scales and investigation of associated subnanometer length scales involved in confined dynamics.[40] In a previous publication, the significance of hydrogen bonds (H-bonds) to the slowing of dynamics was explicated for the structurally similar and also mildly basic imidazole, which can form H-bond chains as a result of having a hydrogen atom instead of a methyl group at the N1 position (see numbering scheme in Figure 1).[38] Although MeIm cannot readily H-bond with itself, it has a large dipole moment of 3.8 D[41] (3.6 D for imidazole) that is comparable to acetonitrile (3.92 D). For context, the dipole moments for water and pore surface silanols are 1.85 and 1.7 D,[42] respectively. The strong dipole−dipole interactions in MeIm[43,44] are demonstrated by its high boiling point (196 °C) compared to nonheterocycles of similar molecular weights (e.g., 80 °C for benzene).[41] In biology, these electrostatic interactions help optimize spatial arrangements of complex molecules, and MeIm-like nitrogen heterocycles are common in nucleic acids.[41,45] MeIm is also a common precursor for imidazolium-based ILs.[46−48] In fact, the first major industrial application of ILs involved using MeIm to scavenge HCl and form an IL that can be easily separated from the desired alkoxyphenylphosphine product (precursor used in UV curable coatings), improving synthetic productivity by a factor of 80,000.[49]

Distance-dependent structural properties, i.e., probability distributions, density, and orientational preferences, of MeIm and $SeCN^-$ were calculated from molecular dynamics (MD) simulations to guide the interpretation of the experimental results and develop analytical models. Because the measured dynamics are spatial averages over the pore interiors, multiple pore sizes were studied to establish the scaling of dynamics with increasing confinement. Obtaining the intrinsic distance dependence of the solvent properties also entails consideration of the spatial distribution of the reporting probe.

In general, the properties of confined liquids are distinctly different from the bulk at distances a few molecular diameters long from the surface of the confining framework. This interfacial layer is the "shell" state in the two-state model interpretation of confined behavior, which describes confined liquids as a sum of a "core" population that resembles the bulk and a distinctive "shell" population near the surface.[40] The width of the interfacial layer and the qualitative changes upon confinement depend on the geometry and surface functionalization, as well as the nature of the confined liquid. In MD simulations of acetonitrile[23,24,28] and water,[17,20,22] when both were confined in silica pores with hydroxylated surfaces, a greater structural order was observed for acetonitrile, which was found to be arranged in antiparallel bilayers. Since MeIm and acetonitrile are both polar and aprotic, similar structural features may induce a similar propagation of effects arising from surface interactions. However, differences are expected due to additional π interactions from the MeIm rings and differences in molecular size and geometry.

Confined dynamics can be described by the two-state model when the shell and core dynamics are independent of the pore size and cleanly separated at a certain distance from the pore surface. Variations of the two-state model have been invoked in both theoretical and experimental studies of liquid dynamics in porous glass and silica materials,[18,22,24,25,27,32] as well as in reverse micelles[7,11] and polymer electrolyte fuel cell membranes.[8] Furthermore, orientational relaxation and spectral diffusion of $SeCN^-$ in water confined in mesoporous silicas have been successfully described with modified two-state models.[22] The spectral diffusion was described by a smoothed step model, deviating from a strict two-state description only slightly, with the shell dynamics transitioning to the core dynamics continuously and not by means of a step discontinuity at the boundary of the interfacial layer. The confined rotational dynamics of the $SeCN^-$ probe deviated more from a conventional two-state model, as the weighting of the shell and core contributions does not abruptly switch at a certain distance from the pore surface; instead, they exhibit an exponential dependence on distance, with continuous acceleration of the dynamics. For both observables, the interfacial layer was determined to be approximately one water molecule thick. Testing whether MeIm provides similar qualitative and quantitative results will provide important insights on the propagation of surface effects for an organic liquid in a hydrophilic pore in which H-bonding to the surface occurs but the MeIm−MeIm interactions are dominated by strong dipolar coupling.

2. EXPERIMENTAL AND THEORETICAL METHODS

2.1. Sample Preparation and Characterization. Four types of samples were studied: 1:200 molar ratio BmimSeCN/MeIm bulk solution and the same solution confined in roughly cylindrical silica mesopores of diameters 2.8 ± 0.1, 5.4 ± 0.5, and 8.3 ± 0.1 nm. 1-Methylimidazole (MeIm, ≥99%, purified by redistillation, ∼25 ppm H_2O) was purchased from Sigma-Aldrich and used as received. The vibrational probe, 1-butyl-3-methylimidazolium selenocyanate (BmimSeCN), was synthesized according to a published procedure[50] from 1-butyl-3-methylimidazolium chloride (IoLiTec, 99% purity) and potassium selenocyanate (Acros Organics, 99% purity), vacuum dried (∼100 mTorr) overnight under gentle heating (∼35 °C), and stored in a nitrogen glovebox. The residual K^+ concentration in the BmimSeCN product was determined to be ∼40 ppm via ICP-MS, giving a negligible 1 K^+ ion per 770,000 MeIm molecules for the concentration of BmimSeCN used. The K^+ concentration dependence of the dynamics is discussed in the Supporting Information (SI). All silica powders were vacuum dried (∼100 mTorr) at ∼190 °C and stored in a nitrogen glovebox. The 2.8 nm (MCM41) and 8.3 nm (SBA15) powders purchased from ACS Material have particle sizes <1 μm and required no additional treatment before drying. The 5.4 nm (SBA15) silica from Sigma Aldrich contained a wide range of particle sizes (up to ∼150 μm) and generated a prohibitive amount of scattered light at the wavelengths used (λ ∼4.8 μm).[39] Smaller particles (<43 μm) were isolated by collecting the top fraction of silica powder suspended in a long column of water after a brief period of

https://doi.org/10.1021/acs.jpcb.1c04798
J. Phys. Chem. B 2021, 125, 10018−10034

sedimentation, as detailed in a previous publication.[39] The pore size distributions, BET surface areas, and pore volumes determined from nitrogen sorption measurements were published previously.[4,22,39]

The 1:200 BmimSeCN/MeIm solution was confined in the pores by a method similar to those described in our previous confinement studies.[4,39] The gravimetrically prepared BmimSeCN/MeIm solution was stirred with the silica powder (~15 min) in a nitrogen glovebox and then vacuum filtered in a nitrogen atmosphere to remove the excess bulk liquid. As the liquid content of the pores varied even with controlled filtration time, the collected powder was equilibrated overnight with a constant flow of MeIm vapor produced by bubbling nitrogen gas through bulk MeIm. Dynamical measurements of the resulting samples were highly reproducible. Percent mass losses observed in thermogravimetric analysis of equilibrated silica powders filled with MeIm solutions had also shown good agreement with theoretical losses for fully filled pores, as calculated from the silica pore volumes and liquid MeIm density.[4]

Once equilibrated, the powder samples were promptly transferred into a nitrogen glovebox and sealed in sample cells. The sample cell assembly consisted of two 3 mm thick, 25.4 mm diameter CaF_2 windows separated by two concentric, 25 μm thick annular Teflon spacers, which simultaneously fixed the sample path length and protected the sample from evaporation and atmospheric moisture. For bulk MeIm, which is hygroscopic, a single Teflon spacer was sufficient to keep the sample well sealed; linear IR spectra of the samples before and after the ultrafast IR experiments showed no discernable differences. For powder samples, an index-matching fluid (paraffin oil) was added to the powder, which was confined within the smaller spacer (inner diameter ~8 mm), and also added to the annular region between the concentric spacers to further ensure sample integrity. Fourier transform infrared (FT-IR) spectra of the samples were collected with a spectrometer purged with air free of CO_2 and H_2O. The absorption spectra of corresponding samples prepared without BmimSeCN were measured and subtracted from the sample spectra.

2.2. Nonlinear Infrared Spectroscopy. Detailed descriptions of the nonlinear spectroscopic techniques used were provided in previous studies on bulk and confined water dynamics;[22,39,51] an overview is presented here. The two-dimensional infrared (2D IR) vibrational echo experiments and polarization selective pump-probe (PSPP) experiments were performed in a pump-probe geometry[52−54] with the 2D IR spectrometer described in previous publications.[51,54] A Ti:Sapphire oscillator/regenerative amplifier, 800 nm with a 1 kHz repetition rate, pumps an OPA to produce ~7 μJ mid-IR pulses centered at 2065 cm^{-1} with ~170 fs full width at half-maximum (FWHM) duration. This resulting mid-IR pulse is split into a strong pump that is directed into an acousto-optic mid-IR pulse shaper[52,54,55] and a weak probe that is sent into a mechanical delay line.

In 2D IR experiments, three time-ordered mid-IR pulses, centered at the resonant frequency of the 0−1 transition (here, for the CN stretch of $SeCN^-$), are crossed in the sample to generate a third-order macroscopic polarization. The first two incident pulses are pump pulses whose amplitudes, phases, and relative time delay, τ, are precisely controlled using a pulse shaper. Pulses 1 and 2, respectively, label and store the initial frequencies, ω_1, of an ensemble of CN stretches. As the MeIm solvent structure evolves over a variable waiting time T_w, the resulting changes in intermolecular interactions between individual MeIm and $SeCN^-$ alter the vibrational frequencies (spectral diffusion) of the CNs within the range of the inhomogeneously broadened absorption line. Pulse 3 (the probe) terminates the structural evolution period, T_w, and stimulates the emission of a fourth pulse, the vibrational echo, which reports the final frequencies, ω_3, of the ensemble. The echo signal is collinear with and heterodyned by the probe pulse, which also serves as the local oscillator (LO). Both are directed into a monochromator, which frequency disperses the beams onto pixels of an IR array detector, effectively performing an experimental Fourier transform to yield the final frequency axis of the 2D spectra, ω_3. Interferograms produced by scanning τ are recorded at each ω_3, and the numerical Fourier transform of these interferograms yields the initial frequency axis of the 2D spectra, ω_1. From the resulting series of 2D spectra (ω_3 vs ω_1) over a range of T_w's, the time dependence of the spectral diffusion of the ensemble of CN stretches and thus the time dependence of solvent structural fluctuations were determined. At early T_w, the 2D spectrum is elongated along the diagonal ($\omega_3 = \omega_1$), indicating a strong correlation between the initial (ω_1) and final (ω_3) frequencies. For increasing T_w, as the CN probes sample more solvent structures, the 2D spectrum becomes rounder, signifying loss of correlation.

This loss of correlation was quantified using the center line slope (CLS) method.[56,57] The CLS(T_w) decay is the normalized frequency−frequency correlation function (FFCF), the probability that a vibrational probe with a given initial frequency exhibits the same frequency at a later time T_w, averaged over all frequencies in the absorption line.[53,56,57] The complete FFCF is usually described by the Kubo model, as follows:[53,58]

$$\mathrm{FFCF} = C_\omega(T_w)\langle\delta\omega(0)^2\rangle = \langle\delta\omega(T_w)\delta\omega(0)\rangle = \frac{\delta(T_w)}{T_2} + \sum_i \Delta_i^2 \exp[-T_w/\tau_i] \quad (1)$$

where $C_\omega(T_w)$ is the normalized FFCF, $\delta\omega(T_w) = \omega(T_w) - \langle\omega\rangle$ is the frequency fluctuation (i.e., the difference between the instantaneous frequency $\omega(T_w)$ and the average frequency $\langle\omega\rangle$), $\delta(T_w)$ is the Dirac delta function, T_2 is the total homogeneous dephasing time, and Δ_i and τ_i are the amplitude of the frequency fluctuation and time constant of the ith decay pathway, respectively. The full FFCF, which has the same time constants as the CLS(T_w), was determined from the CLS(T_w) and the linear absorption spectrum using the recently developed CAFE program. CAFE employs artificial neural networks to quickly and accurately obtain the FFCF parameters, producing results that are accurate for spectral diffusion components in both the homogeneous and inhomogeneous limits.[59]

In PSPP experiments, the time delay τ between pulses 1 and 2 is set to 0, i.e., a single pump pulse, and only T_w (referred to as t) is varied. Using a pump pulse polarized at 45° relative to the probe, the transient intensity differences in the probe, with the pump turned on and off, are measured at both parallel and perpendicular polarizations by resolving the signal at 45° and −45°, respectively,[53,60,61] resulting in parallel $S_\parallel(t)$ and perpendicular $S_\perp(t)$ signals. The isotropic pump-probe decay, $P(t)$ (vibrational lifetime), and the orientational anisotropy, $r(t)$, were obtained using the following equations:[60,61]

https://doi.org/10.1021/acs.jpcb.1c04798
J. Phys. Chem. B 2021, 125, 10018−10034

$$P(t) = [S_{\parallel}(t) + 2S_{\perp}(t)]/3 \quad (2)$$

$$r(t) = \frac{S_{\parallel}(t) - S_{\perp}(t)}{S_{\parallel}(t) + 2S_{\perp}(t)} = 0.4C_2(t) \quad (3)$$

The form of eq 3 is rigorously true only for an isotropic system,[62,63] and the reasons for its applicability for studying these silica pores were previously presented.[51] $C_2(t)$ is the second Legendre polynomial orientational correlation function of the transition dipole moment.[60] Perfect orientational correlation corresponds to $C_2(t) = 1$ and anisotropy $r(t) = 0.4$. Deviations from the value of 0.4 at $t = 0$ are common and are caused by ultrafast inertial orientational motions[64] that are beyond the temporal resolution of the measurements.

These measurements on the strongly light scattering silica powders were made possible by polarization schemes and phase cycling techniques previously described.[39,52,65] The 2D spectra were taken only in the perpendicular polarization such that scattered light resulting from the pump was largely mitigated. Heterodyne scatter in the PSPP data was also reduced by employing a four-shot phase cycle.

3. RESULTS AND DISCUSSION

3.1. IR Experiments. *3.1.1. Linear IR Absorption Spectra.* The background-subtracted linear absorption spectra of $SeCN^-$ in bulk and confined MeIm are presented in Figure 2. The center frequency (2065 cm^{-1}) of the CN stretch is essentially unchanged among bulk and confined systems (Table 1). The FWHMs in all pore sizes studied were identical (14.9 cm^{-1}) and broader than in the bulk (13.8 cm^{-1}). The spectra have a very small red wing, which is slightly reduced upon confinement. The red wing is attributed to the non-Condon effect, or the frequency dependence of the transition dipole strength.[51,66] This effect and the solvatochromism of $SeCN^-$ are discussed in detail in the SI.

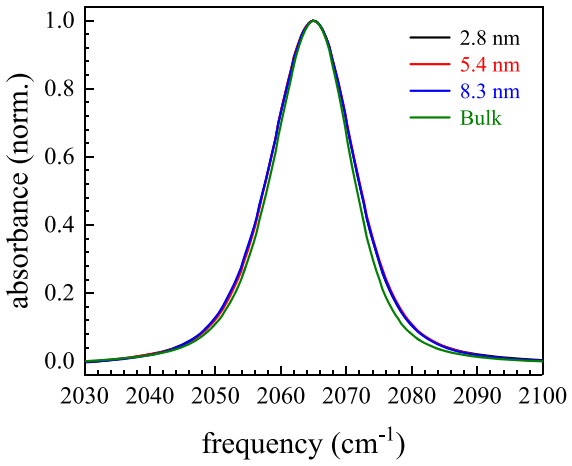

Figure 2. Linear IR spectra of the CN stretch of $SeCN^-$ in bulk MeIm (green curve) and in MeIm confined in silica pores of sizes 8.3 nm (blue curve), 5.4 nm (red curve), and 2.8 nm (black curve). The spectra are more symmetric and slightly broader upon confinement; however, the center frequencies are unchanged from the bulk.

Table 1. Line Shape Parameters and Vibrational Lifetimes

sample	center (cm^{-1})	FWHM (cm^{-1})	lifetime (ps)
2.8 nm	2064.96 ± 0.03	14.9 ± 0.1	102 ± 2
5.4 nm	2064.94 ± 0.04	14.9 ± 0.2	110 ± 2
8.3 nm	2064.98 ± 0.05	14.9 ± 0.1	115 ± 1
bulk	2065.02 ± 0.01	13.8 ± 0.1	143 ± 1

MeIm, though not generally considered as an H-bond donor, had been shown to form very weak H-bonds with $SeCN^-$ via the C2 hydrogen (Figure 1) and occasionally the C4 and C5 hydrogens.[38] The pore surface has at least three distinguishable types of silanols (isolated free, geminal free, and vicinal).[67,68] Interactions between MeIm and the surface silanols can change the H-bonding capacity of MeIm (see the SI for details), giving rise to a broader range of $SeCN^-$ frequencies. Since the center frequency changed negligibly upon confinement, the net H-bonding between $SeCN^-$ and MeIm does not appear to change significantly. The lack of a pronounced blueshift also suggests that the $SeCN^-$ does not directly form the strong and hence blueshifted (see the SI) H-bonds with surface silanols, which is consistent with simulations revealing a tendency for the $SeCN^-$ to avoid the surface ($SeCN^-$ probability distributions in Section 3.2.1).

3.1.2. Isotropic Pump-Probe Decays. The CN stretch vibrational lifetime of $SeCN^-$ in MeIm was obtained from the isotropic pump-probe decays $P(t)$ (see eq 2). Fitting the decays out to 800 ps for nine frequencies (2060.9 to 2070.3 cm^{-1}) revealed two major features. First, dynamics occurring at time scales much faster than the vibrational lifetime were present, with the behavior most apparent in the bulk sample. This is a result of fast spectral diffusion caused by the non-Condon effect,[51,69] as observed for $SeCN^-$ in D_2O.[51] Second, small longtime offsets were observed in the pore samples. However, fitting the $P(t)$ with small offsets produced the same lifetimes as more involved treatments of the offsets as isotropic heating signals.[70−72] More details on the $P(t)$ are in the SI.

With these considerations accounted for, a single, frequency-independent lifetime was obtained for each sample (Table 1). The lifetime is longest in the bulk sample (143 ± 1 ps) and monotonically decreases with confinement to 102 ± 2 ps for the smallest pore size (2.8 nm). A monotonic decrease in $SeCN^-$ lifetime was also observed for D_2O confined in the same pores, but the decrease (~3 ps between bulk and 2.8 nm) was subtle and the pore lifetimes were within error of each other.[51] The dependence of $SeCN^-$ lifetimes on pore size is discussed in Section 3.3.

3.1.3. Orientational Relaxation. The anisotropy decays, $r(t)$ (see eq 3), give the $SeCN^-$ orientational relaxation dynamics in MeIm, providing information on the surrounding MeIm molecules that constrain $SeCN^-$ rotation. In all samples studied, $r(t)$ is frequency independent in the vicinity of the line center and was averaged across nine frequencies (same range as $P(t)$) to improve the signal-to-noise ratio. The $r(t)$ data (points) in Figure 3 are well described by triexponential decays (solid curves) with no offsets, and the fit parameters are given in Table 2. The decays measured in the pores have the same form as the decays in the bulk; i.e., all are triexponentials. The triexponential form of the bulk $r(t)$ can be interpreted in terms of the wobbling-in-a-cone model of restricted orientational diffusion,[73−75] as discussed below. Since the pore measurements are spatially averaged for $SeCN^-$ located at varying distances from the surface, wobbling parameters are not calculated for the pore $r(t)$. While direct comparison of the spatially averaged measurements underestimates the confinement effects, slower dynamics are still evident: a monotonic increase in all three time constants with increasing confine-

https://doi.org/10.1021/acs.jpcb.1c04798
J. Phys. Chem. B 2021, 125, 10018−10034

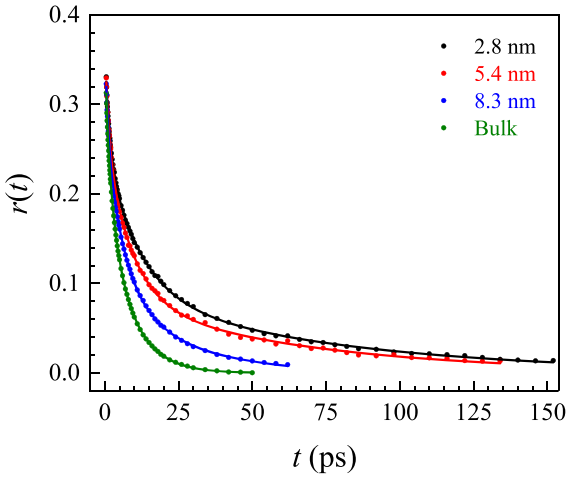

Figure 3. Measured rotational anisotropy decays $r(t)$ of $SeCN^-$ in bulk MeIm (green points) and MeIm confined in silica pores of sizes 8.3 nm (blue points), 5.4 nm (red points), and 2.8 nm (black points). The solid curves are triexponential fits to the data.

ment was observed. A detailed examination of distance dependence of the orientational relaxation is provided in Section 3.3, where $r(t)$ for all pore sizes are fit with a single model involving a weighted sum of core and shell $r(t)$.

A useful parameter to assess confinement effects from the spatially averaged data is the integrated correlation time τ_c, which weights each time scale component by its normalized amplitude,

$$\tau_c = \frac{1}{A(0)} \int_0^\infty A(t)dt \tag{4}$$

with $A(t)/A(0)$ representing the normalized correlation function $C_2(t)$. The bulk τ_c (5.1 ± 0.2 ps) is clearly faster than that for the largest pore size, 8.3 nm (9.6 ± 0.2 ps). For the smaller 5.4 and 2.8 nm pores, τ_c = 20 ± 2 and 23.9 ± 0.7 ps, respectively, are substantially shorter and almost the same. This is an initial indication that the influence of the surface extends a significant distance into the pore. For comparison, the $SeCN^-$ τ_c in bulk D_2O and that in the same 5.4 nm pore are just within error of each other.[22] The ratios of τ_c for 2.8 nm to bulk are ~4.7 for MeIm and ~1.4 for D_2O, suggesting more pronounced confinement effects on the orientational relaxation of $SeCN^-$ in MeIm. From Table 2, t_3, the slowest time constants for complete orientational relaxation, in the bulk MeIm liquid and in the 8.3, 5.4, and 2.8 nm pores are 8.4 ± 0.3, 24 ± 1, 70 ± 6, and 74 ± 2 ps, respectively. Again, the similar 5.4 and 2.8 nm values suggest that the complete reorientation in confined MeIm is dominated by surface effects.

In the wobbling-in-a-cone model, the orientational correlation function $C_2(t)$ is modeled with ultrafast inertial motions; two diffusive time constants, τ_{c1} and τ_{c2}, for two stages of restricted angular diffusion ("wobbling"); and a final time constant, τ_m, for complete orientational randomization:[69]

$$C_2(t) = T^2\{S^2 + (1 - S^2)\exp[-t/\tau_{c1}]\} \{R^2 + (1 - R^2)\exp[-t/\tau_{c2}]\}\exp[-t/\tau_m] \tag{5}$$

The T^2 factor is the square of the generalized order parameter representing the inertial motions. Because this decay is too fast to contribute to the observed dynamics, it does not have an associated time constant.[69] The form of the squared generalized order parameters T^2, S^2, and R^2 is

$$Q^2 = \left[\frac{1}{2}\cos\theta_c(1 + \cos\theta_c)\right]^2 \tag{6}$$

where θ_c is the half angle for a cone of angular space that a CN transition dipole explores. More restricted wobbling motion was described by a smaller cone angle θ_{c1} and shorter time constant τ_{c1}. The corresponding part of $C_2(t)$ in eq 5 decays to a plateau with value S^2. As the solvent structure evolves over time and structural constraints on angular displacement are relaxed, the CN dipole explores a larger angular space described by cone angle θ_{c2} and time constant τ_{c2}. In the absence of other orientational relaxations, $C_2(t)$ would decay to a lower value R^2, consistent with a greater loss in orientational correlation. When all restrictions on angular displacement dissipate, complete orientational randomization occurs, and $C_2(t)$ decays to zero with time constant τ_m. This final orientational relaxation is attributed to small-step free diffusion, and τ_m can be related to the orientational diffusion constant D_m using the Debye model:[60,62,76]

$$D_m = \frac{1}{6\tau_m} \tag{7}$$

The time constants τ_{c1}, τ_{c2}, and τ_m obtained from fitting $r(t)$ with eq 5 are related to the time constants from the general triexponential fit by $\tau_{c1} = t_1$, $\tau_{c2} = (1/t_2 - 1/t_3)^{-1}$, and $\tau_m = t_3$.[69] The inertial cone half angle θ_{in} and the two diffusive cone half angles θ_{c1} and θ_{c2} were calculated correspondingly from the generalized order parameters T, S, and R (eq 6). Cone diffusion constants were obtained from the diffusive cone half angles using the following equation:

$$D_c \cong 7\theta_c^2/24\tau_c \tag{8}$$

which is an excellent approximation for cone half angles ≤30°[77] and in good agreement with the full expression[74] for the values here. To describe the full range of angular space sampled over all periods of restricted orientational diffusion, the total cone half angle θ_{tot} was obtained from the total order

Table 2. Orientational Relaxation Parameters[a]

sample	A_1	t_1 (ps)	A_2	t_2 (ps)	A_3	t_3 (ps)	τ_c (ps)
2.8 nm	0.112 ± 0.004	1.3 ± 0.1	0.165 ± 0.009	11.3 ± 0.4	0.091 ± 0.002	74 ± 2	23.9 ± 0.7
5.4 nm	0.106 ± 0.009	1.3 ± 0.2	0.184 ± 0.005	9.1 ± 0.7	0.079 ± 0.008	70 ± 6	20 ± 2
8.3 nm	0.090 ± 0.004	0.91 ± 0.05	0.180 ± 0.004	5.8 ± 0.2	0.105 ± 0.005	24 ± 1	9.6 ± 0.2
bulk	0.071 ± 0.005	0.42 ± 0.05	0.125 ± 0.006	2.4 ± 0.2	0.202 ± 0.007	8.4 ± 0.3	5.1 ± 0.2

[a]Triexponential fit parameters to the anisotropy for $SeCN^-$ in bulk MeIm and MeIm in silica pores of different sizes. The A_i and t_i are the amplitude and time constant of the ith component. τ_c is the integrated correlation time.

https://doi.org/10.1021/acs.jpcb.1c04798
J. Phys. Chem. B 2021, 125, 10018−10034

Table 3. Wobbling-in-a-Cone Analysis Parameters (Bulk MeIm)[a]

θ_{in} (°)	θ_{c1} (°)	θ_{c2} (°)	θ_{tot} (°)	τ_{c1} (ps)	τ_{c2} (ps)	τ_{m} (ps)	D_{c1} (ps^{-1})	D_{c2} (ps^{-1})	D_{m} (ps^{-1})
4 ± 3	20.5 ± 0.6	31.8 ± 0.9	37.7 ± 0.8	0.48 ± 0.04	3.3 ± 0.2	8.4 ± 0.3	0.075 ± 0.005	0.025 ± 0.002	0.0199 ± 0.0007

[a]See text for parameter descriptions.

parameter Q_{tot} = *TRS* using eq 6. Cone half angles, time constants, and diffusion constants are tabulated in Table 3.

For probes including $SeCN^-$, CO_2, methanol-d_4, and ethanol-d_6 studied in an imidazolium-based IL, the first of two wobbling motions was strongly influenced by the nature of the interactions between the probe and the IL, while the second wobbling motion reflected configurational changes in these interactions as a result of local IL structural changes.[69,78] For $SeCN^-$ in D_2O, one wobbling time scale was observed preceding free diffusion, whereas only free diffusion was observed when using the water hydroxyl as a native probe.[51] In general, the wobbling motions appear to be associated with probe−solvent interactions, whereas the free diffusion reflects inherent solvent properties.

Although MeIm is not charged like an IL nor is it an H-bond donor like water, its large dipole moment allows for H-bonding with $SeCN^-$[38] and gives rise to strong dipole−dipole interactions.[41,43,44] The two cone angles for $SeCN^-$ in MeIm are quite similar to those for $SeCN^-$ in the imidazolium-based IL, suggesting that similar interactions constrain $SeCN^-$ rotation in both liquids.[78] The complete orientational relaxation time, τ_m, is consistent with hydrodynamic predictions using the slip boundary condition (details in the SI).

3.1.4. Spectral Diffusion. In Figure 4, representative 2D spectra at T_w = 0.5 and 15 ps are shown for the smallest pore

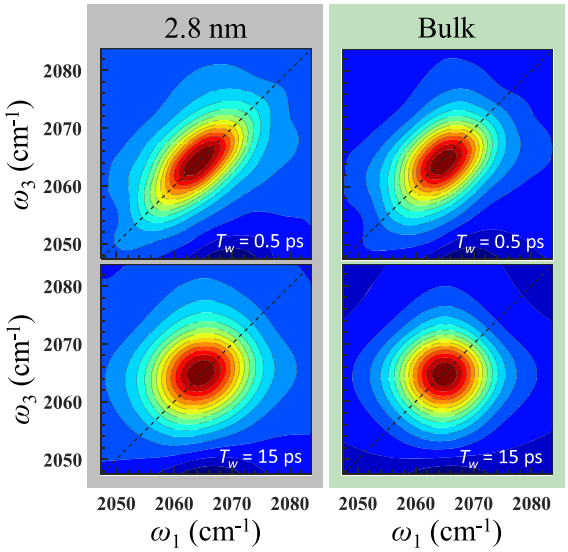

Figure 4. 2D IR spectra of the CN stretch of $SeCN^-$ in bulk MeIm and MeIm confined in 2.8 nm silica pores at time delays T_w = 0.5 and 15 ps. The time dependence of the MeIm structural fluctuations is obtained from the changes in shape of the 2D spectra with T_w.

size (2.8 nm) and the bulk liquid. The shape of the 0−1 transition (red, positive going peak) becomes rounder at the longer T_w, indicating a loss of correlation, which is quantified with the CLS (the normalized FFCF).[56,57] In practice, the CLS(T_w) starts below 1 (with 1 being perfect correlation) at T_w = 0 (Figure 5) due to T_w independent homogeneous broadening. The lower the initial CLS value is, the greater the contribution of homogeneous broadening to the spectral linewidth is.

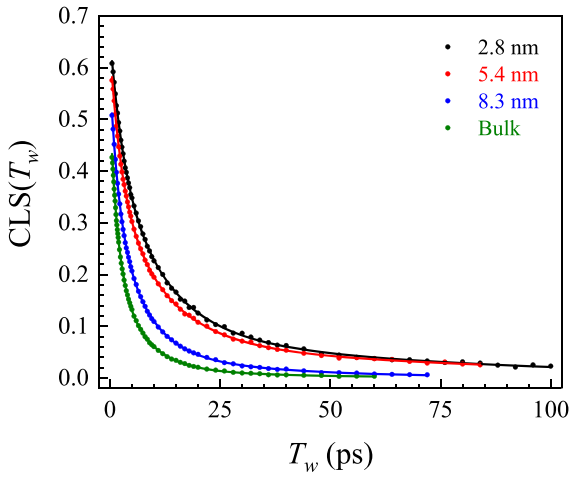

Figure 5. Measured CLS(T_w) decays (spectral diffusion) of the CN stretch of $SeCN^-$ in bulk MeIm (green points) and MeIm confined in silica pores of sizes 8.3 nm (blue points), 5.4 nm (red points), and 2.8 nm (black points). The solid curves are triexponential fits to the data. The CLS decays are the normalized frequency−frequency correlation functions.

The spectral diffusion of $SeCN^-$ in MeIm slows significantly upon confinement. The CLS(T_w) decays (points) shown in Figure 5 were fit with triexponential decays (solid curves) with no offsets, and the fit parameters are given in Table 4. The decay for the largest pore size studied (8.3 nm) is noticeably slower than that of the bulk. For perspective, the ratio of correlation times τ_c for 2.8 nm to bulk CLS is ∼3.4 for MeIm, which is greater than the corresponding ratio of ∼1.4 for D_2O. The τ_c increases with increasing confinement: 4.8 ± 0.2 ps for bulk, 7.2 ± 0.4 ps for 8.3 nm, 15.8 ± 0.4 ps for 5.4 nm, and 16.3 ± 0.7 ps for 2.8 nm. However, unlike the anisotropy, the time scales for the triexponential fits do not increase monotonically with increasing confinement. The time scales for the largest pore size and bulk are within experimental error, and the time scales for the two smaller pore sizes are also within error of each other. The increase of τ_c comes instead from a shift of the amplitude from the short to long time scales with increasing confinement. This may be a sign of a two-state (core and shell) behavior, which is further discussed in Section 3.3. The very similar τ_c for 5.4 and 2.8 nm suggests that the shell behavior extends >2 nm from the surface.

The FFCF can be calculated by simultaneously fitting the CLS(T_w) and the linear absorption spectrum.[53,58,59] While FFCFs can be calculated from the spatially averaged measurements on the pore samples (Table 5), it is not straightforward to decompose the FFCF by distance because there are no distinctive core and shell contributions to the observed linear spectra; the spectra for all pore sizes were identical and barely

https://doi.org/10.1021/acs.jpcb.1c04798
J. Phys. Chem. B 2021, 125, 10018−10034

Table 4. CLS Parameters[a]

sample	A_1	t_1 (ps)	A_2	t_2 (ps)	A_3	t_3 (ps)	τ_c (ps)
2.8 nm	0.22 ± 0.03	2.8 ± 0.3	0.35 ± 0.03	10.8 ± 0.4	0.091 ± 0.003	70 ± 6	16.3 ± 0.7
5.4 nm	0.26 ± 0.02	2.6 ± 0.1	0.31 ± 0.01	11 ± 1	0.07 ± 0.01	85 ± 14	15.8 ± 0.4
8.3 nm	0.24 ± 0.04	1.9 ± 0.3	0.30 ± 0.03	7.1 ± 0.7	0.051 ± 0.008	33 ± 6	7.2 ± 0.4
bulk	0.28 ± 0.01	1.63 ± 0.03	0.22 ± 0.01	6.2 ± 0.2	0.024 ± 0.004	29 ± 6	4.8 ± 0.2

[a]Triexponential fit parameters to the CLS for $SeCN^-$ in bulk MeIm and MeIm in silica pores of different sizes. The A_i and t_i are the amplitude and time constant of the ith component. τ_c is the integrated correlation time.

Table 5. FFCF Parameters[a]

sample	T_2 (ps)	Γ (cm^{-1})	Δ_1 (cm^{-1})	t_1 (ps)	Δ_2 (cm^{-1})	t_2 (ps)	Δ_3 (cm^{-1})	t_3 (ps)
2.8 nm	3.0 ± 0.1	3.6 ± 0.1	3.8 ± 0.2	2.8 ± 0.3	4.0 ± 0.2	10.8 ± 0.4	1.89 ± 0.03	70 ± 6
5.4 nm	3.0 ± 0.1	3.5 ± 0.2	4.3 ± 0.2	2.6 ± 0.1	3.7 ± 0.1	11 ± 1	1.7 ± 0.2	85 ± 14
8.3 nm	3.0 ± 0.3	3.5 ± 0.4	4.5 ± 0.1	1.9 ± 0.3	3.7 ± 0.2	7.1 ± 0.7	1.4 ± 0.1	33 ± 6
bulk	3.0 ± 0.3	3.6 ± 0.4	4.8 ± 0.1	1.63 ± 0.03	3.0 ± 0.1	6.2 ± 0.2	0.88 ± 0.07	29 ± 6

[a]T_2: observed homogeneous dephasing time; $\Gamma = 1/\pi T_2$: homogeneous line width; Δ_i and τ_i: frequency fluctuation amplitude and time constant for the ith component, respectively.

different from the bulk spectrum. The near identity of the bulk and pore spectra was also observed for $SeCN^-$ in D_2O.[22]

The time constants τ_i of the FFCF (Table 5) represent different decay pathways and are the same as those reported for the triexponential fits to the CLS(T_w) (Table 4). Compared to the normalized amplitudes in the CLS(T_w), the frequency fluctuation amplitudes Δ_i in the FFCF are in frequency units (cm^{-1}). The CLS(T_w) and FFCF can be determined from both parallel and perpendicular polarization 2D IR data. Under circumstances where reorientation-induced spectral diffusion (RISD) occurs,[79−81] the perpendicular and parallel CLS(T_w) curves have different decays. For $SeCN^-$ in bulk MeIm, the differences between parallel and perpendicular CLS(T_w) decays are small (SI Figure S5).[38] Thus, the RISD contribution to the spectral diffusion is minor and will not be considered for either the bulk or pore samples. All CLS(T_w) and FFCF parameters presented were extracted from 2D spectra acquired in the scatter-reducing, perpendicular polarization. Further discussion of the FFCF is in the SI.

Previous experiments provide some insights into the nature of the motions that give rise to the different time scale dynamics observed. The spectral diffusion of $SeCN^-$ in bulk MeIm had been compared to a structurally similar molecule, imidazole, at the same temperature (both in liquid state at 95 °C).[38] Unlike the primarily H-bond accepting MeIm, imidazole is amphiprotic and can form extended H-bond networks, mainly chains. The spectral diffusion time scales, while longer for imidazole, were within error for the two liquids. However, the overall dynamics in MeIm are faster than in imidazole because the amplitudes of the faster time scale components are larger for MeIm. This difference in amplitudes suggests that spectral diffusion occurs through similar physical processes but to different extents. A possible explanation is that strong dipole−dipole interactions present in MeIm[41,43,44] may result in substantial intermolecular coupling somewhat analogous to the H-bond interactions in the imidazole.

The intermediate time scale (6.2 ps) in MeIm may be related to fast fluctuations involving the imidazole ring and is comparable to the fast time scales observed for imidazolium ILs with various alkyl chain lengths, which ranged from 5 to 12 ps depending on the vibrational probe used.[82,83] The fastest time scale observed (1.63 ps) is slower than the time scales (0.3−0.6 ps) associated with very local H-bond length fluctuations observed for $SeCN^-$ in ILs and water,[51,69,84,85] but may reflect analogous local dynamics in MeIm.

3.2. Simulations: Liquid Structure. The observed slowing of $SeCN^-$ dynamics in MeIm with decreasing pore size reflects changes in the nature of the MeIm liquid structure and the manner in which $SeCN^-$ interacts with the altered liquid structure. The effects of the pore surface vary with distance, and the measurements are a function of both the MeIm dynamics at a given position and the probability that a $SeCN^-$ probe molecule is at that position to report on those dynamics. In general, confined liquid dynamics at silica pore surfaces are slower than the bulk and dynamics at the center are typically comparable to the bulk.[22,24,27,29,40]

As confined liquids tend to be organized in layers radiating outward from the wall of a confining framework,[23,24,40] it is useful to quantify the extent of the liquid layering and the thickness of a liquid layer when analyzing the dynamical measurements. MD simulations were performed to compute the probability distribution, density, and orientation of the molecules confined in the silica pores. Details regarding constructing and populating the silica pores are given in the SI. The bulk and pore $r(t)$ calculated using the model pore systems gave reasonable agreement with experimentally measured $r(t)$ (SI Figure S6). The simulations of the liquid structure as a function of distance from the pore surface helped to guide the analysis and interpretation of the experimental results.

3.2.1. Structural Layering. In Figure 6, the normalized probability distributions $f(d)$ of MeIm and $SeCN^-$ are given for the three pore sizes studied. For a circular cross section of a nominally infinitely long cylindrical pore, the $f(d)$ distribution is defined as the probability of finding a molecule in an annular region a distance d from the pore surface. Such distributions are usually given as a function of d instead of the radial distance ρ from the pore center since the position of the surface with respect to the pore center varies with surface roughness, making distributions based on radial distances less well defined. At any given position, the sum of the distances d and ρ is the pore radius R (1.4, 2.7, or 4.15 nm). Accordingly, $f(d)$ goes to zero as d approaches R since the available volume at the pore center (i.e., $\rho = 0$) is zero. Normalization ensures that the total probability of finding a molecule in the circular cross section is unity; i.e., the integral of $f(d)$ is 1. For MeIm, d

https://doi.org/10.1021/acs.jpcb.1c04798
J. Phys. Chem. B 2021, 125, 10018−10034

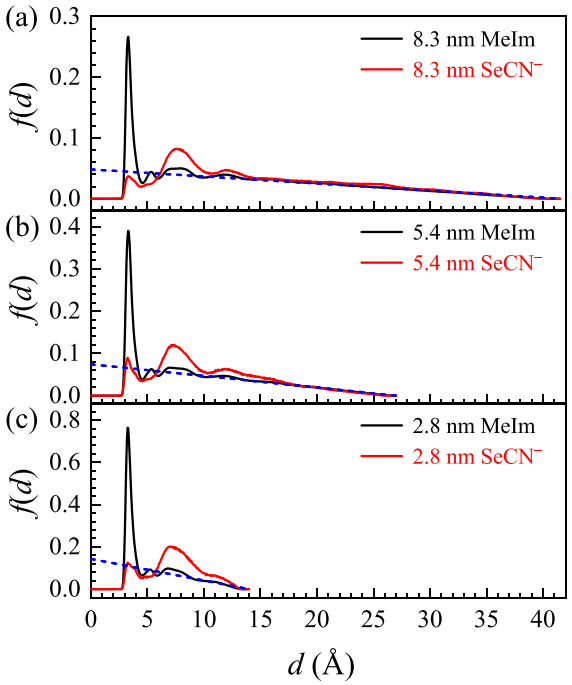

Figure 6. Normalized probability distributions $f(d)$ for the MeIm C2 atom (black) and $SeCN^-$ carbon atom (red) as a function of the distance d from the pore surface in (a) 8.3 nm, (b) 5.4 nm, and (c) 2.8 nm pores. The blue dashed lines represent uniform distributions.

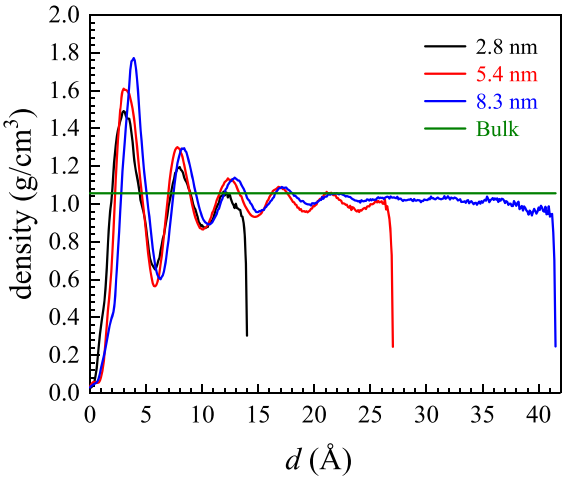

Figure 7. Density profiles for MeIm as a function of the distance d from the pore surface in 8.3 nm (blue), 5.4 nm (red), and 2.8 nm (black) pores. The horizontal green line corresponds to bulk MeIm density. The oscillations reflect the layering of MeIm induced by the surface.

is defined as the minimum distance between the MeIm ring C2 atom (Figure 1) and the nearest pore O atom. For $SeCN^-$, it is the minimum distance between the nitrile C atom and the nearest pore O atom. There is zero probability between d = 0 and 2.6 Å since that space is intrinsically occupied by the atoms and bonds between the centers of the two reference atoms that define d. This reference value d_0 = 2.6 Å will be used in Section 3.3 and is comparable to the ∼3 Å extracted from the $f(d)$ for $SeCN^-$ in D_2O confined in mesoporous silica.[22] For all pore sizes, MeIm probability is peaked close to the surface, consistent with the MeIm densities shown in Figure 7, which also show a dense layer near the surface.

For a uniform (bulk-like behavior) distribution of molecules, one would expect $f(d)$ to decrease linearly with d, as the ratio of the annular region to the total available space increases linearly with ρ with the form $\frac{2\pi\rho}{\pi R^2} = \frac{2\rho}{R^2}$. In Figure 6, the blue dashed lines corresponding to uniform distributions are overlaid on the calculated $f(d)$. Comparing the decaying MeIm probability oscillations (black traces) with the blue dashed lines, four distinct MeIm layers can be identified in all pore sizes followed by unstructured, bulk-like liquid in the pore interior (except in the smallest pore size). The amplitude decays of the oscillating densities (Figure 7) toward the bulk density (horizontal green line) also show at least four MeIm layers (only three can be observed for the smallest pore size) followed by the bulk-like behavior. The dip in the density at the pore center is an artifact of counting molecules in very small volumes. A similar structural layering has been observed at acetonitrile silica interfaces.[23,86] Water has fewer distinct layers.[17,22] In simulations, acetonitrile layering was observed even when the pore surface was rendered non-H-bonding or not charged.[23,24] Steric effects are then key to liquid layering, which is likely why layering in water propagates shorter distances compared to that of the larger acetonitrile and MeIm molecules.[40]

The $SeCN^-$ $f(d)$ (red traces in Figure 6) also exhibits multiple layers before tending toward a bulk-like behavior at the pore interior. However, the $SeCN^-$ probability peaks farther from the surface, with the second local maximum having a larger amplitude than the first. Since the measurement of the MeIm dynamics is weighted by the $SeCN^-$ distribution, these simulated distributions are important references for the model fits in Section 3.3.

To quantify the surface effects in the measured dynamics, it is useful to define the interfacial thickness Δ. A reasonable reference value of Δ = 4.6 Å is obtained from the value of d at the first minimum in the $f(d)$ distribution and the peak-to-peak distance for MeIm density. This value is similar to the molecular diameter of 5.02 Å obtained for MeIm treated as a perfect sphere with a volume of 66.2 $Å^3$ (calculated using the Connolly volume computation method with a probe radius of zero).[87]

3.2.2. Orientational Structure. In Figure 8, the average orientation of MeIm in the three pore sizes is shown. These traces are overlaid on the normalized orientational density distribution $F(d, \cos\theta)$ of MeIm confined in the 8.3 nm pore. We defined a vector between the two ring N atoms, going from N1 to N3 (Figure 1). An angle θ can be measured between this vector and the radial vector extending from the pore center toward the surface. For this definition, $\cos\theta = 1$ corresponds to the nitrogen lone pair on N3 pointing toward the surface. No distinction is made for the cone of orientations at each θ. For example, for $\cos\theta = 0$, depending on the orientation of the imidazole ring, the ring may be lying flat (parallel to the surface), or it may be perpendicular to the surface, with the methyl group on N1 pointing either toward or away from the surface. These ambiguities aside, it is still clear from Figure 8 that there is a preference for the N3 lone pair to point closer to the surface ($\cos\theta > 0$) in the first layer of MeIm molecules and for the next layer to be oriented antiparallel ($\cos\theta < 0$) to the first. The bilayer feature persists for at least another pair of layers, though the effects are not obvious in the contour plot

https://doi.org/10.1021/acs.jpcb.1c04798
J. Phys. Chem. B 2021, 125, 10018−10034

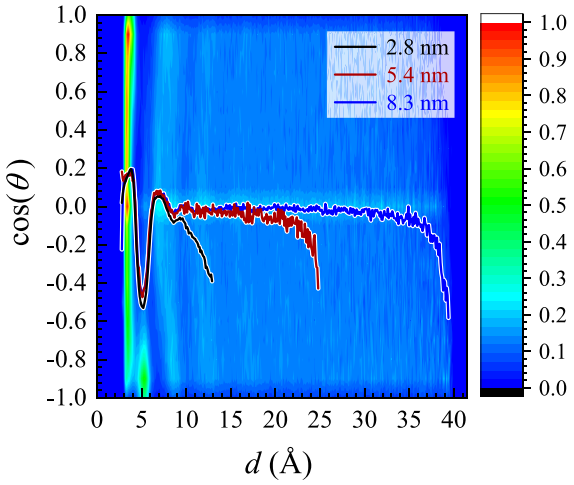

Figure 8. Contour plot of the orientational density distribution $F(d, \cos\theta)$ of MeIm confined in an 8.3 nm pore. The overlaid lines are the average orientation as a function of the distance d from the pore surface in 8.3 nm (blue curve), 5.4 nm (red curve), and 2.8 nm (black curve) pores.

due to the overwhelming probability of finding MeIm adjacent to the surface (Figure 6).

The bilayers in MeIm are more clearly visualized by the alternating sign of the average orientations (solid lines in Figure 8). The dips near the pore center arise for the same reason as the dips in the density plots. In simulations, antiparallel ordering of acetonitrile occurred even in the absence of explicit H-bonds but not when the surface was methylated or set to zero charge, highlighting the significance of surface dipoles on the orientational ordering of polar species like acetonitrile.[23,24,32] In contrast, water is only weakly ordered near the surface, and ordering does not propagate far from the surface.[17,22] These differences may be a result of a more unidirectional dipole pairing of acetonitrile, compared to water, which forms approximately tetrahedral H-bond networks.[23,24] It is reasonable then that MeIm, which, like acetonitrile, also has a large dipole moment and is generally only H-bond accepting, is also arranged in antiparallel bilayers with the N3 lone pair in the first layer pointed toward the surface. Calculations of MeIm orientation on a quartz surface (with silanol surface groups) based on sum frequency generation (SFG) measurements also suggest that the main interaction between MeIm and the silanol surface is H-bonding via the N3 lone pair.[88] The nitrogen lone pair on 4-picoline, a similar nitrogen heterocycle, also forms weak H-bonds with silanol OH groups on silica surfaces.[89] While the sp^2 lone pair on the N3 atom of MeIm should be more H-bond donating than the N1 lone pair, which is delocalized into the aromatic ring, weak H-bonding to the N1 atom is still possible,[88] explaining the lack of an overwhelming preference for the N3 atom to be closer to the surface. The orientational preference may be further reduced by π H-bonding interactions between the ring electrons and the surface, which were shown in MD simulations of benzene, a nonpolar aromatic species, to result in the benzene rings lying flat on the silica surface.[29]

$SeCN^-$ (solid red line in SI Figure S7) is similarly arranged in an antiparallel fashion, with the first layer showing a preference for the N lone pairs to point toward the surface, most likely due to H-bonding as well. However, the relative probability of $SeCN^-$ to be in the first layer is much lower than for MeIm (Figure 6). Furthermore, the first antiparallel layer of $SeCN^-$ corresponds to a local minimum in the $SeCN^-$ probability distribution (SI Figure S7). This $f(d)$ minimum for $SeCN^-$ overlaps with a maximum for its counteraction, $Bmim^+$ (SI Figure S8), which has a periodicity similar to MeIm.

Given the low concentration of BmimSeCN used, it is unlikely that either ion has a significant influence on the MeIm structure, but their probability distributions are likely affected by MeIm. If the interactions between $SeCN^-$ with the surface were substantially preferred over the interactions between MeIm with the surface, we would expect a substantial fraction of the $SeCN^-$ to be located at and bonded to the surface. Based on the $SeCN^-$ concentration and typical silanol density on the surface (2 OH groups/nm^2),[90] the number of silanols on the surface greatly outnumbers the number of $SeCN^-$ in a pore, with a ratio of 26:1 for the largest pore size and 77:1 for the smallest pore size. The exclusion of $SeCN^-$ from the surface may be a result of the MeIm bilayer acting like a phospholipid in a biological membrane, preventing ion passage through its hydrophobic interior. Though also charged, $Bmim^+$ has a hydrophobic alkyl chain, which may be the reason for its higher probability near the surface.

3.3. Scaling of Dynamics with Size. *3.3.1. Modified Two-State Models.* Confined dynamics are often interpreted using a two-state, or core−shell, model to relate the measured properties to molecular behavior.[7,8,11,18,22,24,25,27,32] The underlying assumption is that the dynamical property of interest, D, takes on one value at the surface ("shell" state) and another in the pore interior ("core" state). The core behavior is often taken to be the same as the bulk. A key assumption is that the distance dependence of the dynamics is independent of the size of the confining framework, meaning that the dynamics in different pore sizes can be treated as a weighted sum of the same constituents. For $SeCN^-$ dynamics in confined D_2O, simulated dynamics (orientational relaxation and spectral diffusion) at varying distances from the silica pore surface were indeed identical for different pore sizes.[22] Without similar simulations, it is unclear if the assumption applies for MeIm. The success of our two-state model fits (Figure 9) suggests that it is reasonable. Furthermore, computational studies of other organic liquids such as acetonitrile and benzene indicated that the distance dependences of the confined reorientational dynamics were insensitive to the pore diameter.[24,29] The rate constant of a reaction involving MeIm in silica pores was also well described by a two-state model.[4] Nonetheless, caution should be exercised when interpreting and comparing the effects of confinement on different properties of a liquid.

To establish a baseline for the more elaborate model fits, the measured lifetime, anisotropy, and CLS data were first fit with the simplest two-state model, independent of system details gleaned from the simulated liquid structures. Assuming a uniform $SeCN^-$ distribution, the pore data were fit as a weighted sum of core and shell dynamics, with the former fixed to the bulk parameters and the latter varied. The proportion of the shell contribution scales with the area of the annular shell region with variable thickness Δ relative to the circular cross section. The best fits gave a shell thickness of $\Delta \sim 10.4$ Å or roughly two MeIm layers. The fits clearly miss the experimental data (SI Figure S9), which is unsurprising given that the simulated $SeCN^-$ distributions are far from uniform. Furthermore, the three different dynamical variables may not

https://doi.org/10.1021/acs.jpcb.1c04798
J. Phys. Chem. B 2021, 125, 10018−10034

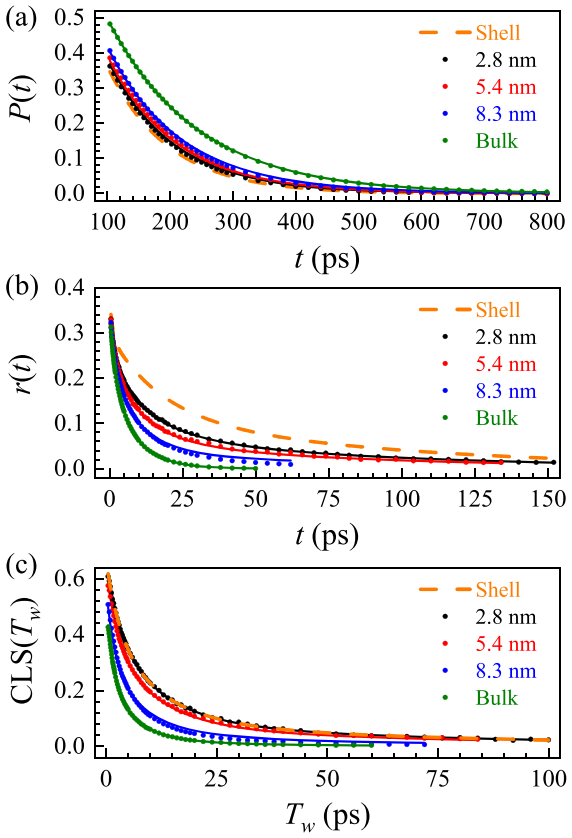

Figure 9. Measured (a) isotropic pump-probe lifetime decays $P(t)$, (b) rotational anisotropies $r(t)$, and (c) CLS(T_w) decays (spectral diffusion) of $SeCN^-$ in bulk MeIm (green points) and MeIm confined in silica pores of sizes 8.3 nm (blue points), 5.4 nm (red points), and 2.8 nm (black points). The solid curves of the same colors are modified two-state model fits to the data. The orange dashed curves are the model shell decays that yield the best fit to the experimental data (distance averaged data) for the three pore sizes.

necessarily obey the strict two-state model with the same spatial dependence.

The modified two-state model fits made use of information from the simulations of the liquid structure. The distributions $f(\rho)$ representing the probability of finding $SeCN^-$ in an annular region (with radius ρ in a cross section of a pore with radius R) were modeled as a skewed sine squared distribution over one period $\rho = [0, R - d_0]$:

$$f(\rho) = A\rho^a \sin^2[\pi\rho/(R - d_0)] \times \theta[R - d_0 - \rho] \quad (9)$$

These tunable distributions capture key characteristics of the simulated $SeCN^-$ probability distribution but smooth out the fine structure. At $\rho = 0$ (the pore center), the probability is zero. As per the simulated results, the distributions are peaked near the surface and have zero probability from $\rho = R - d_0$ to $\rho = R$. The value of d_0 is fixed to the value of 2.6 Å obtained from the simulations, but floating the parameter also resulted in values that were within error. The only variable parameter a captures the skew of the distribution. The minimum value $a = 0$ describes a distribution peaked halfway between $\rho = 0$ and $\rho = R - d_0$. Increasing values of a shift the peak closer toward the surface. The coefficient A is a normalization constant to ensure that $\int_0^R f(\rho)d\rho = 1$.

The spatially averaged, time-dependent dynamical variable $D(t; R)$ (the measured observable) is a function of the position- and time-dependent dynamical variable $D(t; \rho)$, weighted by the probability distribution $f(\rho)$ of $SeCN^-$ probes sensing those dynamics:

$$D(t; R) = \int_0^R D(t; \rho) f(\rho) d\rho \quad (10)$$

The integrand $D(t; \rho)$ is a weighted sum of the core and shell functions:

$$D(t; \rho) = D_{core}(t) + [D_{shell}(t) - D_{core}(t)] \times m(\rho) \quad (11)$$

The weighting factor $m(\rho)$ models the variation of the specific dynamical variable with radial distance ρ, and different functional forms of $m(\rho)$ may be necessary for different dynamical observables since they are sensitive to different aspects of the system. The expanded form of eq 10 after taking the distance-independent components (core and shell functions) out of the integral is then

$$D(t; R) = D_{core}(t) + [D_{shell}(t) - D_{core}(t)] \int_0^R m(\rho) \times f(\rho) d\rho \quad (12)$$

For $SeCN^-$ dynamics in confined D_2O, $m(\rho)$ for the $r(t)$ and CLS(T_w) was an exponential decay and a smoothed step function, respectively.[22] The lifetime was not modeled in the D_2O study since the differences were quite small. Below is the $D(t; \rho)$ for the lifetime, anisotropy, and CLS in the MeIm systems, with the corresponding $m(\rho)$ being a smoothed step, an exponential, and a normal step:

$$P(t; \rho) = P_{core}(t) + [P_{shell}(t) - P_{core}(t)] \times \frac{1}{2}\left(\tanh\left[\frac{\Delta_P - (R - d_0 - \rho)}{\alpha}\right] + 1\right) \quad (13)$$

$$r(t; \rho) = r_{core}(t) + [r_{shell}(t) - r_{core}(t)] \times e^{-(R - d_0 - \rho)/\xi} \quad (14)$$

$$CLS(T_w; \rho) = CLS_{core}(T_w) + [CLS_{shell}(T_w) - CLS_{core}(T_w)] \times \theta[\Delta_{CLS} - (R - d_0 - \rho)] \quad (15)$$

There are two variable parameters for the smoothed step function in eq 13: the shell thickness Δ_P, which defines the position of the step at $\rho = R - d_0 - \Delta_P$ (or $d = d_0 + \Delta_P$), and the smoothness parameter α, which determines how abrupt the transition is between shell and core behaviors. Larger values of α correspond to a smoother transition, and small values approaching zero yield a normal step function. For the exponential decay model in eq 14, there is one variable parameter, the characteristic length ξ. The normal step model in eq 15 is a shifted Heaviside function with one variable parameter, the shell thickness Δ_{CLS}, which defines the position of the step in the same manner as Δ_P.

To determine the combination of models that would most accurately describe the data, the data sets were fit individually and simultaneously with all permutations of the three models. Differences between visually similar fits were quantified by the Akaike Information Criterion (AIC) values, which consider both the residual sum of squares and the number of fitting parameters.[91] The number of exponentials used in the shell correlation functions for $r(t)$ and CLS(T_w) was kept to the minimum necessary. Fitting the three types of data

https://doi.org/10.1021/acs.jpcb.1c04798
J. Phys. Chem. B 2021, 125, 10018−10034

simultaneously proved to be the most important constraint. The fits of individual data sets to different models were often of similar quality. However, while the models describing the transition from shell to core dynamics may differ with the observable, the system itself should be invariant, meaning that the $SeCN^-$ $f(\rho)$ for a given pore size should be identical regardless of the dynamics being measured. The models that we settled on (eqs 13−15) gave the best agreement among different sets of $f(\rho)$ obtained for individual fits and the set of shared $f(\rho)$ in a global fit of all three dynamical variables. This shared set of $f(\rho)$ (dashed lines in Figure 10) have means,

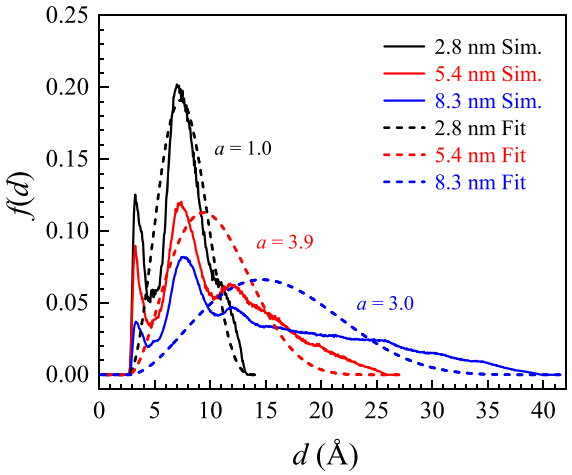

Figure 10. Normalized probability distributions for $SeCN^-$ as a function of the distance d from the pore surface as determined through simulations (solid curves) and from the modified two-state model fits to the measured dynamics (dashed lines) for 2.8 nm (black), 5.4 nm (red), and 8.3 nm (blue) pores. The skew parameters, a, describe the degree that the distributions lean toward the surface.

medians, and modes consistent with the simulated $f(\rho)$ (solid lines in Figure 10). The values of the skew parameter a are 1.0 ± 0.5, 3.9 ± 0.8, and 3.0 ± 0.1 for the 2.8, 5.4, and 8.3 nm pores, respectively. Directly applying the simulated $f(\rho)$ gave poorer fits but resulted in parameters and shell decay curves that were within error bars of those produced by the sine squared distribution fits, indicating that the nature of the system derived from the experimental results is in good agreement with simulations. Accounting for the lifetime variation of $SeCN^-$ located at different distances resulted in global fits that are very slightly better than those without the lifetime corrections, and the resulting parameters and shell dynamics (Table 6) are essentially identical to those obtained without this correction. This was expected since the lifetimes are long with respect to the dynamical time scales being considered. For such long-lived probes, their spatial diffusion may result in an exchange between core and shell populations, but the displacements are negligible on the time scales of the dynamics beings studied. Specifics of the lifetime correction procedure and the negligible effects of exchange are given in the SI.

3.3.2. Physical Insights and Comparisons to Confined Water. In Figure 11, the three models $m(\rho)$ describing the

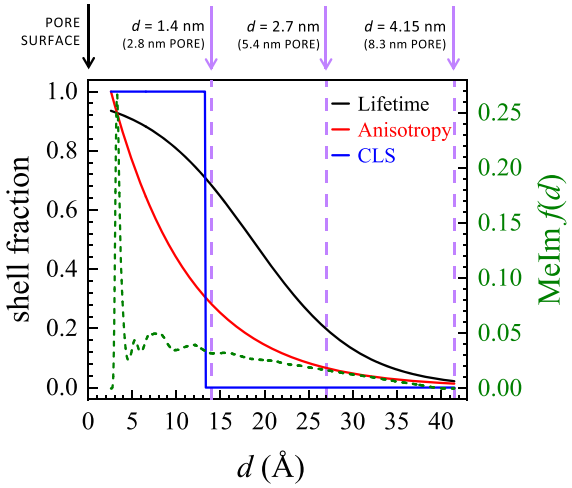

Figure 11. Plots of the smoothed step (black), exponential decay (red), and simple step (blue) models, as a function of the distance d from the pore surface, describing the transitions between shell and core characteristics for the vibrational lifetime, anisotropy, and CLS, respectively. The green dashed curve (right axis, reproduced from Figure 6) is the simulated probability distribution of MeIm. The dashed purple lines mark the centers of the 2.8, 5.4, and 8.3 nm pores.

transitions between shell and core lifetime $P(t)$, anisotropy $r(t)$, and CLS (T_w) are plotted as functions of the distance d from the pore surface. The plot extends to the radius of the 8.3 nm pore but applies to all pore sizes when truncated at the corresponding distances marking the respective pore centers (purple dashed lines). The smoothed step function (black curve) that describes the transition between the shell and core (bulk) lifetimes is defined by an interfacial thickness $\Delta_P = 16 \pm 2$ Å and a smoothness parameter $\alpha = 12 \pm 3$ Å. For the anisotropy (red curve), the transition is modeled by an exponential decay with a characteristic length $\xi = 9 \pm 1$ Å. The transition for the CLS (blue curve) is a simple step function, with $\Delta_{CLS} = 10.7 \pm 0.1$ Å. These interfacial thicknesses and characteristic lengths obtained from the model fits are on the order of two to three MeIm layers, which was also the case for the shell thickness $\Delta \sim 10.4$ Å obtained from the strict two-state model (step function for all variables, uniform $SeCN^-$ distributions).

Table 6. Core and Shell Dynamics from Modified Two-State Model Fits

observable	A_1	t_1 (ps)	A_2	t_2 (ps)	A_3	t_3 (ps)	τ_c (ps)
$P_{core}(t)$[a]		143 ± 1					
$P_{shell}(t)$		98 ± 3					
$r_{core}(t)$[a]	0.071 ± 0.005	0.42 ± 0.05	0.125 ± 0.006	2.4 ± 0.2	0.202 ± 0.007	8.4 ± 0.3	5.1 ± 0.2
$r_{shell}(t)$	0.09 ± 0.01	0.9 ± 0.3	0.18 ± 0.02	18 ± 3	0.12 ± 0.01	92 ± 11	37 ± 2
$CLS_{core}(T_w)$[a]	0.28 ± 0.01	1.63 ± 0.03	0.22 ± 0.01	6.2 ± 0.2	0.024 ± 0.004	29 ± 6	4.8 ± 0.2
$CLS_{shell}(T_i)$	0.24 ± 0.02	3.0 ± 0.1	0.35 ± 0.01	11.4 ± 0.7	0.086 ± 0.007	75 ± 4	16.5 ± 0.2

[a]These values were fixed to the bulk parameters in the fits.

https://doi.org/10.1021/acs.jpcb.1c04798
J. Phys. Chem. B 2021, 125, 10018−10034

The values describing the shell layer, normalized by the MeIm molecular diameter, are larger than the corresponding ones for confined D_2O.[22] In the confined D_2O study, the $r(t)$ curves were also fit to an exponential model, with ξ = 2.0 Å, and the CLS was fit to a smoothed step model with Δ_{CLS} = 2.8 Å and α_{CLS} = 0.75 Å.[22] These ξ and Δ_{CLS} values are on the order of one D_2O molecular diameter (~2.5 Å). The effects of the surface propagate farther for confined MeIm. The $r(t)$ for both liquids was fit with an exponential model, but the characteristic length for MeIm is more than four times longer, which is similar to the relationship between the ratios of the 2.8 nm and bulk $r(t)$ correlation times τ_c (~4.7 for MeIm and ~1.4 for D_2O). Although the CLS was modeled with a normal step function for MeIm and a smoothed step for D_2O, the parameter Δ in both describes the location of the step, which is again almost four times greater for MeIm. This is also comparable to the ratios of the CLS τ_c (~3.4 for MeIm and ~1.4 for D_2O). It should be noted that the CLS for MeIm can also be fit with a steep (small α_{CLS}) smoothed step function, but there is no improvement in the fit.

Using Δ = 4.6 Å as the thickness of one MeIm layer and pore diameters 2.8, 5.4, and 8.3 nm, a corresponding maximum of 3, 6, and 9 MeIm layers can be accommodated in the pores. In the smallest pore, which can only accommodate three layers, the model fit parameters suggest that the measured dynamics should reflect a mostly shell behavior. Indeed, the fitted shell lifetime of 98 ± 3 ps is within error of the spatially averaged 102 ± 2 ps lifetime measured for the 2.8 nm pore. The shell correlation function for the CLS is identical to the triexponential fit to the 2.8 nm CLS, suggesting that, in the smallest pore size, only the shell state spectral diffusion is present. This is not true for $r(t)$, where the $r(t)$ shell correlation function is a more slowly decaying triexponential than the triexponential fit to the 2.8 nm $r(t)$. The shell properties are tabulated in Table 6 and also shown as orange dashed lines in Figure 9. Given these fit parameters and information on the solvent structure from the simulations, some interesting relationships can be inferred between the confined structure and dynamics.

3.3.2.1. Lifetime, P(t). The location of the step at $d = d_0 + \Delta_P$ = 18.6 Å in the gradual transition from the shell to bulk lifetime (Figure 11, black curve) is approximately where the MeIm $f(d)$ (green dashed line) begins to decrease linearly (i.e., unstructured, bulk-like MeIm). This also corresponds to where distinct density oscillations (Figure 7) have subsided, roughly three to four MeIm layers in. The ~45 ps difference in the shell and core lifetimes suggests that the pronounced structural layering of MeIm near the surface has a significant effect on $SeCN^-$ vibrational relaxation. For confined D_2O, the very slight reduction of the $SeCN^-$ lifetime in confined water is then likely a result of the weaker and shorter range structural ordering.[22]

The vibrational lifetime is a very local property sensitive to the immediate solvent environment of the moiety undergoing the vibrational relaxation. For polyatomic chromophores like $SeCN^-$, there are two vibrational relaxation pathways: intramolecular vibrational energy redistribution (IVR) to other modes of the probe itself and intermolecular vibrational energy relaxation (VER) to solvent modes. Given the large energy mismatch between the CN stretch (2065 cm^{-1}) and the C−Se stretch and bend frequencies (560 and 420 cm^{-1}, respectively, in KBr and Nujol mulls),[92] the IVR relaxation pathway alone is inefficient, and intermolecular MeIm bath modes, e.g., librations and translations, will be involved in solvent assisted IVR pathways.[93,94] The deposition of energy from the CN moiety into the bath modes depends on the coupling strength and the density of states, both of which are influenced by the immediate solvent environment. Therefore, a change in the lifetime as the liquid structure transitions from interface influenced to bulk-like is reasonable.

In a computational study focusing on VER of a model diatomic anion solute in a dipolar solvent confined in hydrophobic cavities, the vibrational lifetime decreased monotonically with confinement, decreasing by a factor of ~1.3 from bulk to a 3 nm pore,[95] similar to the ~1.4 factor reduction for $SeCN^-$ in MeIm from bulk to a 2.8 nm pore. The study showed that increasing confinement reduced the vibrational lifetime by increasing the overlap between the solute probability distribution and the solvent density peaks, resulting in increased short-range Lennard−Jones interactions that increased the number of effective VER collisions. Although the cavities in the computational study were spherical and hydrophobic, confinement-enhanced VER should also be important for MeIm confined in silica. As shown in computational studies of confined acetonitrile, unlike orientational ordering, which is also dependent on surface (electrostatic) interactions, the development of high density solvent peaks is primarily a geometric effect.[23] The smooth step model suggests that the most densely packed MeIm interacting with the surface gives rise to the shortest, most shell-like, $SeCN^-$ lifetimes. This shell character persists with only a gradual change at small distances from the surface due to the perpetuation of surface properties. As the layering subsides, the $SeCN^-$ lifetime changes more rapidly, but not sharply, since the local environment, while approaching bulk behavior, is still different from the bulk. Continuing further into the pore interior, as surface effects wane, the MeIm becomes essentially bulk-like, but it is likely that for the very local solute−solvent interactions, there are still discernable differences from the bulk, leading to the slow approach to the core lifetime. As seen in Figure 11, at a distance d = 14 Å (corresponding to the center of a 2.8 nm pore), the lifetime takes on a primarily shell character, corresponding to the only slightly longer average lifetime of 102 ± 2 ps measured for 2.8 nm pores versus the shell lifetime of 98 ± 3 ps from the fits.

3.3.2.2. Anisotropy, r(t). The shell $r(t)$ obtained from the fits (orange dashed line in Figure 9b) decays much more slowly than the bulk, with a 7-fold increase in τ_c. The longest time scale of the triexponential shell $r_{shell}(t)$, which results from the relaxation of all constraints on rotational motion, is ~11 times slower than that of the bulk (Table 6). Given that the size and shape of the reorienting molecule ($SeCN^-$) and temperature remain unchanged, the hydrodynamic theory would suggest that the slowing of shell dynamics is directly proportional to the increase in the effective viscosity. For a bulk MeIm viscosity of 1.72 cP,[38] the effective shell viscosity would be ~19 cP. Both confinement-induced increases in the liquid viscosity and additional structural constraints such as stronger solvent interactions can result in a slower reorientation near the surface.

Of the three models presented here, the exponential transition from shell to core for $r(t)$ (Figure 11, red curve) deviates most from a conventional two-step model. In the limit of large pore sizes and uniform probe distributions, the dependence of a spatially averaged dynamical property on the pore radius R is actually strikingly similar for an exponential

https://doi.org/10.1021/acs.jpcb.1c04798
J. Phys. Chem. B 2021, 125, 10018−10034

model with a characteristic length ξ and a simple step model with a shell thickness ξ. Both expressions are dominated by a leading term $2\xi/R$, indicating that different models based on qualitatively different physical descriptions of the liquid structure can give very similar results. Nonetheless, the very good fits and associated $SeCN^-$ distributions strongly support the use of the exponential model. The characteristic length ξ = 9 Å also provides a meaningful measure of surface effects.

The exponential model had been previously applied to the orientational dynamics of $SeCN^-$ in water confined in the same silica pores.[22] Detailed MD simulations showed that at any given time, t, the value of $C_2(t)$ decreases exponentially with distance from the surface with the same characteristic length ξ for the two simulated pore sizes. A similar exponential decrease with distance was also observed in a computational study of water dynamics in reverse micelles (RMs), but the characteristic lengths were dependent on the RM size, meaning that the shell dynamics (assumed to be invariant in the two-state model) may be slowed by the effects of both the surface and the curvature.[12] This additional influence, i.e., curvature, weakens for larger RMs but was not observed for the silica pores possibly due to the cylindrical pores having one less dimension of confinement.

The continuous change in the $r(t)$ (exponential dependence) instead of a binary (step) or near-binary (smoothed step) change suggests that the rotational dynamics reflect surface effects that decay relatively slowly with distance. Compared to the vibrational lifetime, which depends on the immediate environment of the CN moiety, rotation of the $SeCN^-$ requires the surrounding MeIm molecules to displace to allow the $SeCN^-$ to assume an orientation that occupies space previously filled by the solvent. In the case of $SeCN^-$ rotational dynamics in D_2O, ξ = 2 Å and the shell $r(t)$ was a single exponential decay with a time scale ∼3 times slower than the slower of two bulk time constants, suggesting that the wobbling component observed in the bulk was either low in amplitude or absent near the surface.[22] In contrast, for MeIm, the weight of the amplitudes for the faster (wobbling) time scales increased in the shell $r(t)$. These differences seem to reflect a fundamental difference in the effects of confinement on the two liquids. For water, which already forms extensive H-bond networks in the bulk, the silanol surface groups do not offer a significant change in the types and strengths of interactions present. However, these silanol groups are tethered to a confining framework, making them immobile partners that can severely restrict the rotation of water molecules at the surface. Restriction at the surface is consistent with the characteristic length being on the order of one water molecule and the much slower complete reorientation time dominating the shell behavior. The generally aprotic MeIm, however, gains protic character via H-bonding with the surface. The slowing of both the wobbling and complete reorientation time scales is then directly and indirectly induced by stronger H-bonds between $SeCN^-$ and MeIm. The longer correlation length (9 Å) in MeIm reflects a more directed propagation of surface effects through the antiparallel MeIm layers compared to the tetrahedral network of water molecules.

The importance of the surface silanols to the slowing of $SeCN^-$ rotational dynamics in MeIm is also demonstrated by the relationship of different structural and dynamical features with the types of surface interactions involved. In computational studies of acetonitrile in pores with different surface functionalities, structural layering occurred independent of surface functionality and antiparallel ordering was present as long as the surface was charged, but significantly frustrated rotational dynamics emerged only in the presence of H-bonding silanol surface groups.[23,24] For both the MeIm probability distribution (Figure 6) and density (Figure 7), three to four distinct layers were observed and oscillations extend out to almost 20 Å. This is comparable to the location of the step at ∼18.6 Å describing the lifetime. The MeIm orientational probability plots (Figure 8) show clear orientational preferences for two antiparallel bilayers out to ∼12 Å. The exponential model describing the distance dependence of $r(t)$ is characterized by ξ = 9 Å, corresponding to a distance from the surface $d = d_0 + \xi$ = 11.6 Å.

3.3.2.3. Spectral Diffusion, CLS(T_w). The triexponential shell CLS(T_w) obtained from the model fits (Table 6) is within error of the measured triexponential 2.8 nm CLS(T_w) (Table 4). This suggests that the aspects of the solvent structure that influence spectral diffusion are shell-like throughout the 2.8 nm pore. Thus, the simple step model (Figure 11, blue curve) was sufficient to describe the CLS(T_w) distance dependence. The location of the step at $d = d_0 + \Delta_{CLS}$ = 13.3 Å is close to where the orientational ordering subsides. The interfacial thickness Δ_{CLS} ∼10.7 Å is approximately two MeIm molecules, which is thicker than the value Δ ∼2.8 Å (about one water molecule) obtained for the smoothed step model fit to the $SeCN^-$ CLS(T_w) decays in D_2O.[22] The biexponential shell CLS(T_w) in water was believed to be the slower version of the biexponential bulk water CLS(T_w), with the first time scale reflecting very local H-bond length and angle fluctuations and the second characterizing H-bond dissociation and formation. The triexponential shell CLS(T_w) in MeIm is likely also a slower version of the triexponential bulk CLS(T_w). The larger interfacial thickness for MeIm should be the result of the more unidirectional and, hence, longer range propagation of the dipole ordering in MeIm layers in contrast to the three-dimensional H-bonding in water.

The step function for the CLS(T_w) (Figure 11, blue curve) occurs when the structured nature of the MeIm has essentially ended (Figure 11, green dashed line). The position of the step indicates that the structural fluctuations of the MeIm that are responsible for spectral diffusion are distinct for the surface ordered liquid. It is telling that the position of the step is consistent with the extent of orientational ordering (Figure 8), which reflects the range over which electrostatic directing is prominent. As suggested above, H-bonding with the surface enhances the H-bonding character of MeIm, and these effects can constrain $SeCN^-$ rotation through stronger H-bonds and through slower motions of neighboring MeIm molecules. However, these effects fall off with distance, giving rise to the exponential decay of the fraction of the $SeCN^-$ influenced by the surface. For the lifetime, which is very sensitive to the liquid structure immediately surrounding the CN moiety, the surface influence falls off much more slowly than the other two observables. This may suggest that small differences in the MeIm liquid structure still exist at relatively long distances from the surface, and the lifetime is more sensitive to these differences than the other two observables.

There is an important difference between the 2D IR CLS(T_w) observable and the other two observables. The lifetime is an intramolecular dynamic process of the vibrational probe. It is sensitive to the local structure of the surrounding liquid, but it does not directly report on liquid dynamics. The anisotropy is a measurement of the dynamics of the probe and

https://doi.org/10.1021/acs.jpcb.1c04798
J. Phys. Chem. B 2021, 125, 10018−10034

is influenced indirectly by the solvent dynamics. In contrast to the other two observables, the 2D IR spectral diffusion is a direct result of the solvent dynamics. The time-dependent change in solvent structure changes the vibrational frequencies of the CN stretch. The time dependence of the structural changes will depend on the nature of the average liquid structure and is thus the most direct measurement of the solvent structural dynamics as a function of distance from the surface.

4. CONCLUDING REMARKS

The effects of confinement on the polar aprotic liquid, 1-methylimidazole, in silica pores of varying diameters (2.8, 5.4, and 8.3 nm) were investigated by vibrational spectroscopic measurements of the CN stretch of $SeCN^-$ dissolved in MeIm. FT-IR, polarization selective pump-probe experiments, and 2D IR spectroscopy generated the corresponding observables: linear absorption spectra, vibrational lifetimes and orientational relaxation, and spectral diffusion. MD simulations of the probability distribution, density, and orientational ordering of MeIm and $SeCN^-$ provided structural information as a function of distance from the pore surface. The simulations guided the development and interpretation of analytical two-state models used to describe the confined dynamics.

Analysis of the bulk MeIm observables in comparison with those in imidazole,[38] ILs,[78] and water[51] revealed that H-bonding of $SeCN^-$ and MeIm is present and relevant. Despite being aprotic and mildly basic, MeIm can still donate H-bonds via the H atom at the C2 position and, to a lesser extent, the C4 and C5 H atoms (Figure 1).[38] The nature and number of these H-bonds appear to change under confinement as a result of additional H-bonding interactions between the confined MeIm and the silanol surface. These changes were reflected in the broadened linear spectrum and—with increasing confinement—shorter vibrational lifetime, slower rotational dynamics, and slower spectral diffusion.

The simulated structural properties of confined MeIm are very similar to those of acetonitrile, another polar aprotic solvent, confined in hydrophilic silica pores.[23,24,28] Compared to confined water,[17,22] confined MeIm exhibits greater structural ordering, with three to four distinct liquid layers and antiparallel bilayers that begin with the MeIm closest to the surface preferentially orienting their N3 atoms toward the surface. The $SeCN^-$ distributions in the silica pores are also structured and peaked near, but not at, the surface. Since the spatial distributions of the probe directly determine the representation of different solvent layer dynamics in the spatially averaged measurements, they were included in the modeling of the distance dependence of the dynamics.

Modified two-state model fits to the measured dynamics produced parameters consistent with shell-like dynamics propagating through three to four MeIm layers as compared to one layer for D_2O.[22] The distance dependences of these quantities were assumed to be independent of pore size, in accordance with simulations of other organic liquids confined in mesoporous silica.[24,29] The analytical form of the transition (the modification to the two-state model) as a function of distance from the pore surface varies with the observable. The vibrational lifetime is described by a smoothed step transition between a shorter shell lifetime and a core (bulk) lifetime, with an interfacial thickness $\Delta_P \sim 16$ Å that is related to the extent of liquid layering. Orientational relaxation speeds up exponentially with increasing distance from the surface and becomes bulk-like at the pore center for the larger pore sizes. The exponential transition is characterized by a shorter length $\xi \sim 9$ Å, consistent with a dependence on shorter-range surface interactions such as H-bonds. Of the three observables, spectral diffusion is most directly related to the intrinsic liquid dynamics and structure and conforms best to a conventional two-state model, with a step transition at $\Delta_{CLS} \sim 10.7$ Å sharply separating shell and core behaviors.

Given the similar qualitative descriptions of the core−shell transition of $SeCN^-$ dynamics in both the aprotic MeIm and protic D_2O, it is likely that the physical implications apply to a range of liquids. The success of the models in reproducing the pore-size-dependent experimental data highlights the importance of surface functionalities and the nature of the confined liquid to the propagation of surface-influenced dynamics. Confinement in hydrophilic pores clearly has a larger effect on MeIm, which, unlike water, lacks extensive H-bond networks in the bulk liquid but engages in H-bonds with the surface and experiences strong dipole ordering under confinement. The greater extent of surface effects for MeIm described by the model fits is in accord with the relative increase in surface-induced structural order shown in the simulations. As discussed in detail, the different observables are sensitive to distinct aspects of the MeIm liquid structure and dynamics. The molecular-level pictures presented by the different two-state models are based on analytical approximations to the spatial distributions obtained from the simulations. While it is important to recognize that these models smooth out details of the MeIm ordering induced by the surface, they are useful for fitting the experimental data and providing well-defined functional forms for the spatial dependence of the different observables. Studies of ultrafast confined dynamics in liquids other than water are scarce, so the understanding of the scaling of dynamics with pore size will benefit from additional studies on liquids with different molecular dimensions and interactions with surface moieties.

■ ASSOCIATED CONTENT

Supporting Information

The Supporting Information is available free of charge at https://pubs.acs.org/doi/10.1021/acs.jpcb.1c04798.

Simulation methods, solvatochromism and non-Condon effects, isotropic pump probe signals, probe concentration dependence, hydrodynamic theory, bulk CLS decays in different polarization configurations, FFCF parameters, simulated anisotropies, $SeCN^-$ orientational probability, $Bmim^+$ probability distributions, simple two-state model fits, and lifetime and exchange considerations for model fits (PDF)

■ AUTHOR INFORMATION

Corresponding Authors

Weizhong Zheng − *State Key Laboratory of Chemical Engineering, East China University of Science and Technology, Shanghai 200237, China;* orcid.org/0000-0002-3866-4932; Phone: (021) 64253175; Email: wzzheng@ecust.edu.cn

Michael D. Fayer − *Department of Chemistry, Stanford University, Stanford, California 94305, United States;* orcid.org/0000-0002-0021-1815; Phone: (650) 723-4446; Email: fayer@stanford.edu

Authors

Samantha T. Hung − *Department of Chemistry, Stanford University, Stanford, California 94305, United States;* orcid.org/0000-0001-9448-0962

Steven A. Yamada − *Department of Chemistry, Stanford University, Stanford, California 94305, United States;* orcid.org/0000-0003-3171-1625

Complete contact information is available at: https://pubs.acs.org/10.1021/acs.jpcb.1c04798

Notes

The authors declare no competing financial interest.

■ ACKNOWLEDGMENTS

This work was funded by the Division of Chemical Sciences, Geosciences, and Biosciences, Office of Basic Energy Sciences of the U.S. Department of Energy through Grant DE-FG03-84ER13251 (S.T.H., S.A.Y., and M.D.F.) and the National Natural Science Foundation of China (22008065) (W.Z.). S.T.H. gratefully acknowledges partial support from the Marks Family Graduate Fellowship Fund. S.A.Y. gratefully acknowledges partial support from a Stanford Graduate Fellowship.

■ REFERENCES

(1) Kinsey, T.; Glynn, K.; Cosby, T.; Iacob, C.; Sangoro, J. Ion Dynamics of Monomeric Ionic Liquids Polymerized In Situ within Silica Nanopores. *ACS Appl. Mater. Interfaces* **2020**, *12*, 44325−44334.

(2) Chen, X.; Put, B.; Sagara, A.; Gandrud, K.; Murata, M.; Steele, J. A.; Yabe, H.; Hantschel, T.; Roeffaers, M.; Tomiyama, M.; Arase, H.; Kaneko, Y.; Shimada, M.; Mees, M.; Vereecken, P. M. Silica Gel Solid Nanocomposite Electrolytes with Interfacial Conductivity Promotion Exceeding the Bulk Li-ion Conductivity of the Ionic Liquid Electrolyte Filler. *Sci. Adv.* **2020**, *6*, eaav3400.

(3) Minakata, S.; Komatsu, M. Organic Reactions on Silica in Water. *Chem. Rev.* **2009**, *109*, 711−724.

(4) Zheng, W.; Yamada, S. A.; Hung, S. T.; Sun, W.; Zhao, L.; Fayer, M. D. Enhanced Menshutkin S_N2 Reactivity in Mesoporous Silica: The Influence of Surface Catalysis and Confinement. *J. Am. Chem. Soc.* **2020**, *142*, 5636−5648.

(5) Mohamedali, M.; Ibrahim, H.; Henni, A. Imidazolium Based Ionic Liquids Confined into Mesoporous Silica MCM-41 and SBA-15 for Carbon Dioxide Capture. *Microporous Mesoporous Mater.* **2020**, *294*, 109916.

(6) Dokter, A. M.; Woutersen, S.; Bakker, H. J. Inhomogeneous Dynamics in Confined Water Nanodroplets. *Proc. Natl. Acad. Sci. U. S. A.* **2006**, *103*, 15355−15358.

(7) Piletic, I. R.; Moilanen, D. E.; Spry, D. B.; Levinger, N. E.; Fayer, M. D. Testing the Core/Shell Model of Nanoconfined Water in Reverse Micelles Using Linear and Nonlinear IR Spectroscopy. *J. Phys. Chem. A* **2006**, *110*, 4985−4999.

(8) Moilanen, D. E.; Piletic, I. R.; Fayer, M. D. Water Dynamics in Nafion Fuel Cell Membranes: The Effects of Confinement and Structural Changes on the Hydrogen Bond Network. *J. Phys. Chem. C* **2007**, *111*, 8884−8891.

(9) Musat, R.; Renault, J. P.; Candelaresi, M.; Palmer, D. J.; Le Caër, S.; Righini, R.; Pommeret, S. Finite Size Effects on Hydrogen Bonds in Confined Water. *Angew. Chem., Int. Ed.* **2008**, *47*, 8033−8035.

(10) Castrillón, S. R.-V.; Giovambattista, N.; Aksay, I. A.; Debenedetti, P. G. Evolution from Surface-Influenced to Bulk-Like Dynamics in Nanoscopically Confined Water. *J. Phys. Chem. B* **2009**, *113*, 7973−7976.

(11) Moilanen, D. E.; Fenn, E. E.; Wong, D.; Fayer, M. D. Water Dynamics in Large and Small Reverse Micelles: From Two Ensembles to Collective Behavior. *J. Chem. Phys.* **2009**, *131*, No. 014704.

(12) Pieniazek, P. A.; Lin, Y. S.; Chowdhary, J.; Ladanyi, B. M.; Skinner, J. L. Vibrational Spectroscopy and Dynamics of Water Confined inside Reverse Micelles. *J. Phys. Chem. B* **2009**, *113*, 15017−15028.

(13) Singh, P. K.; Kuroda, D. G.; Hochstrasser, R. M. An Ion's Perspective on the Molecular Motions of Nanoconfined Water: A Two-Dimensional Infrared Spectroscopy Study. *J. Phys. Chem. B* **2013**, *117*, 9775−9784.

(14) Bakulin, A. A.; Cringus, D.; Pieniazek, P. A.; Skinner, J. L.; Jansen, T. L. C.; Pshenichnikov, M. S. Dynamics of Water Confined in Reversed Micelles: Multidimensional Vibrational Spectroscopy Study. *J. Phys. Chem. B* **2013**, *117*, 15545−15558.

(15) Yuan, R.; Yan, C.; Nishida, J.; Fayer, M. D. Dynamics in a Water Interfacial Boundary Layer Investigated with IR Polarization Selective Pump-Probe Experiments. *J. Phys. Chem. B* **2017**, *121*, 4530−4537.

(16) Chowdhary, J.; Ladanyi, B. M. Molecular Dynamics Simulation of Aerosol-OT Reverse Micelles. *J. Phys. Chem. B* **2009**, *113*, 15029−15039.

(17) Milischuk, A. A.; Ladanyi, B. M. Structure and Dynamics of Water Confined in Silica Nanopores. *J. Chem. Phys.* **2011**, *135*, 174709.

(18) Laage, D.; Thompson, W. H. Reorientation Dynamics of Nanoconfined Water: Power-Law Decay, Hydrogen-Bond Jumps, and Test of a Two-State Model. *J. Chem. Phys.* **2012**, *136*, No. 044513.

(19) Bourg, I. C.; Steefel, C. I. Molecular Dynamics Simulations of Water Structure and Diffusion in Silica Nanopores. *J. Phys. Chem. C* **2012**, *116*, 11556−11564.

(20) Milischuk, A. A.; Ladanyi, B. M. Polarizability Anisotropy Relaxation in Nanoconfinement: Molecular Simulation Study of Water in Cylindrical Silica Pores. *J. Chem. Phys.* **2014**, *141*, 18C513.

(21) Burris, P. C.; Laage, D.; Thompson, W. H. Simulations of the Infrared, Raman, and 2D-IR Photon Echo Spectra of Water in Nanoscale Silica Pores. *J. Chem. Phys.* **2016**, *144*, 194709.

(22) Yamada, S. A.; Hung, S. T.; Thompson, W. H.; Fayer, M. D. Effects of Pore Size on Water Dynamics in Mesoporous Silica. *J. Chem. Phys.* **2020**, *152*, 154704.

(23) Morales, C. M.; Thompson, W. H. Simulations of Infrared Spectra of Nanoconfined Liquids: Acetonitrile Confined in Nanoscale, Hydrophilic Silica Pores. *J. Phys. Chem. A* **2009**, *113*, 1922−1933.

(24) Cheng, L.; Morrone, J. A.; Berne, B. J. Structure and Dynamics of Acetonitrile Confined in a Silica Nanopore. *J. Phys. Chem. C* **2012**, *116*, 9582−9593.

(25) Norton, C. D.; Thompson, W. H. On the Diffusion of Acetonitrile in Nanoscale Amorphous Silica Pores. Understanding Anisotropy and the Effects of Hydrogen Bonding. *J. Phys. Chem. C* **2013**, *117*, 19107−19114.

(26) Milischuk, A. A.; Ladanyi, B. M. Polarizability Anisotropy Relaxation in Nanoconfinement: Molecular Simulation Study of Acetonitrile in Silica Pores. *J. Phys. Chem. B* **2013**, *117*, 15729−15740.

(27) Norton, C. D.; Thompson, W. H. Reorientation Dynamics of Nanoconfined Acetonitrile: A Critical Examination of Two-State Models. *J. Phys. Chem. B* **2014**, *118*, 8227−8235.

(28) Thompson, W. H. Structure, Dynamics and Hydrogen Bonding of Acetonitrile in Nanoscale Silica Pores. *Mol. Simul.* **2015**, *41*, 788−794.

(29) Coasne, B.; Fourkas, J. T. Structure and Dynamics of Benzene Confined in Silica Nanopores. *J. Phys. Chem. C* **2011**, *115*, 15471−15479.

(30) Falkowska, M.; Bowron, D. T.; Manyar, H.; Youngs, T. G. A.; Hardacre, C. Confinement Effects on the Benzene Orientational Structure. *Angew. Chem., Int. Ed.* **2018**, *57*, 4565−4570.

(31) Dervin, D.; O'Malley, A. J.; Falkowska, M.; Chansai, S.; Silverwood, I. P.; Hardacre, C.; Catlow, C. R. A. Probing the Dynamics and Structure of Confined Benzene in MCM-41 Based Catalysts. *Phys. Chem. Chem. Phys.* **2020**, *22*, 11485−11489.

(32) Loughnane, B. J.; Farrer, R. A.; Scodinu, A.; Fourkas, J. T. Dynamics of a Wetting Liquid in Nanopores: An Optical Kerr Effect

Study of the Dynamics of Acetonitrile Confined in Sol-Gel Glasses. *J. Chem. Phys.* **1999**, *111*, 5116−5123.
(33) Zhang, J.; Jonas, J. NMR Study of the Geometric Confinement Effects on the Anisotropic Rotational Diffusion of Acetonitrile-d_3. *J. Phys. Chem.* **1993**, *97*, 8812−8815.
(34) Beck, J. S.; Vartuli, J. C.; Roth, W. J.; Leonowicz, M. E.; Kresge, C. T.; Schmitt, K. D.; Chu, C. T. W.; Olson, D. H.; Sheppard, E. W.; McCullen, S. B.; et al. A New Family of Mesoporous Molecular Sieves Prepared with Liquid Crystal Templates. *J. Am. Chem. Soc.* **1992**, *114*, 10834−10843.
(35) Kresge, C. T.; Leonowicz, M. E.; Roth, W. J.; Vartuli, J. C.; Beck, J. S. Ordered mesoporous molecular sieves synthesized by a liquid-crystal template mechanism. *Nature* **1992**, *359*, 710−712.
(36) Zhao, D.; Feng, J.; Huo, Q.; Melosh, N.; Fredrickson, G. H.; Chmelka, B. F.; Stucky, G. D. Triblock Copolymer Syntheses of Mesoporous Silica with Periodic 50 to 300 Angstrom Pores. *Science* **1998**, *279*, 548−552.
(37) Suydam, I. T.; Boxer, S. G. Vibrational Stark Effects Calibrate the Sensitivity of Vibrational Probes for Electric Fields in Proteins. *Biochemistry* **2003**, *42*, 12050−12055.
(38) Shin, J. Y.; Wang, Y.-L.; Yamada, S. A.; Hung, S. T.; Fayer, M. D. Imidazole and 1-Methylimidazole Hydrogen Bonding and Nonhydrogen Bonding Liquid Dynamics: Ultrafast IR Experiments. *J. Phys. Chem. B* **2019**, *123*, 2094−2105.
(39) Yamada, S. A.; Shin, J. Y.; Thompson, W. H.; Fayer, M. D. Water Dynamics in Nanoporous Silica: Ultrafast Vibrational Spectroscopy and Molecular Dynamics Simulations. *J. Phys. Chem. C* **2019**, *123*, 5790−5803.
(40) Thompson, W. H. Perspective: Dynamics of Confined Liquids. *J. Chem. Phys.* **2018**, *149*, 170901.
(41) Pozharskii, A. F.; Soldatenkov, A. T.; Katritzky, A. R., Why Nature Prefers Heterocycles. In *Heterocycles in Life and Society*; John Wiley: West Sussex, 2011; pp. 11−33.
(42) Guermeur, R.; Jacolin, C. Influence of Surface Silanols on the Dielectric Properties of Nitrogen Adsorbed on Activated Silica. *Surf. Sci.* **1994**, *315*, 323−336.
(43) Liu, J.-C.; Jia, G.-Z. Dielectric Relaxation of 1-Methylimidazole-Ethanol Mixtures at the Microwave Frequency. *Colloid Polym. Sci.* **2015**, *293*, 2053−2059.
(44) Jia, G.-Z.; Liu, J.-C.; Yang, X.-Q. The Hydrogen Bonding Analysis of 1-Methylimidazole−Water Mixtures Studied by Dielectric Relaxation Spectroscopy. *Fluid Phase Equilib.* **2014**, *375*, 269−274.
(45) Matsuda, A.; Obi, K.; Miyasaka, T. Reaction of Uracil Nucleosides with 1-Methylimidazole in the Presence of Phosphoryl Chloride: A Convenient Method for the Synthesis of 4-Substituted Pyrimidin-2 (1H)-one Nucleosides. *Chem. Pharm. Bull.* **1985**, *33*, 2575−2578.
(46) Verevkin, S. P.; Zaitsau, D. H.; Emel'yanenko, V. N.; Paulechka, Y. U.; Blokhin, A. V.; Bazyleva, A. B.; Kabo, G. J. Thermodynamics of Ionic Liquids Precursors: 1-Methylimidazole. *J. Phys. Chem. B* **2011**, *115*, 4404−4411.
(47) Reiter, J.; Vondrák, J.; Michálek, J.; Mička, Z. Ternary Polymer Electrolytes with 1-Methylimidazole Based Ionic Liquids and Aprotic Solvents. *Electrochim. Acta* **2006**, *52*, 1398−1408.
(48) Holbrey, J. D.; Turner, M. B.; Reichert, W. M.; Rogers, R. D. New Ionic Liquids Containing an Appended Hydroxyl Functionality from the Atom-Efficient, One-Pot Reaction of 1-Methylimidazole and Acid with Propylene Oxide. *Green Chem.* **2003**, *5*, 731−736.
(49) Pozharskii, A. F.; Soldatenkov, A. T.; Katritzky, A. R., Heterocycles and Twenty-First Century Challenges. In *Heterocycles in Life and Society*; John Wiley: West Sussex, 2011; pp. 275−323.
(50) Solangi, A.; Bond, A. M.; Burgar, I.; Hollenkamp, A. F.; Horne, M. D.; Rüther, T.; Zhao, C. Comparison of Diffusivity Data Derived from Electrochemical and NMR Investigations of the $SeC\bar{N}$/$(SeCN)_2$/$(SeCN)_3^-$ System in Ionic Liquids. *J. Phys. Chem. B* **2011**, *115*, 6843−6852.
(51) Yamada, S. A.; Thompson, W. H.; Fayer, M. D. Water-Anion Hydrogen Bonding Dynamics: Ultrafast IR Experiments and Simulations. *J. Chem. Phys.* **2017**, *146*, 234501.
(52) Shim, S.-H.; Zanni, M. T. How to Turn Your Pump-Probe Instrument into a Multidimensional Spectrometer: 2D IR and Vis Spectroscopies via Pulse Shaping. *Phys. Chem. Chem. Phys.* **2009**, *11*, 748−761.
(53) Hamm, P.; Zanni, M. *Concepts and Methods of 2D Infrared Spectroscopy*; Cambridge University Press: New York, 2011.
(54) Kumar, S. K.; Tamimi, A.; Fayer, M. D. Comparisons of 2D IR Measured Spectral Diffusion in Rotating Frames using Pulse Shaping and in the Stationary Frame using the Standard Method. *J. Chem. Phys.* **2012**, *137*, 184201.
(55) Shim, S.-H.; Strasfeld, D. B.; Fulmer, E. C.; Zanni, M. T. Femtosecond Pulse Shaping Directly in the Mid-IR Using Acousto-Optic Modulation. *Opt. Lett.* **2006**, *31*, 838−840.
(56) Kwak, K.; Park, S.; Finkelstein, I. J.; Fayer, M. D. Frequency-Frequency Correlation Functions and Apodization in Two-Dimensional Infrared Vibrational Echo Spectroscopy: A New Approach. *J. Chem. Phys.* **2007**, *127*, 124503.
(57) Kwak, K.; Rosenfeld, D. E.; Fayer, M. D. Taking Apart the Two-Dimensional Infrared Vibrational Echo Spectra: More Information and Elimination of Distortions. *J. Chem. Phys.* **2008**, *128*, 204505.
(58) Kubo, R., In *Fluctuation, Relaxation and Resonance in Magnetic Systems*; Haar, D. T., Ed.; Oliver and Boyd: London, 1961.
(59) Hoffman, D. J.; Fayer, M. D. CLS Next Gen: Accurate Frequency−Frequency Correlation Functions from Center Line Slope Analysis of 2D Correlation Spectra Using Artificial Neural Networks. *J. Phys. Chem. A* **2020**, *124*, 5979−5992.
(60) Tokmakoff, A. Orientational Correlation Functions and Polarization Selectivity for Nonlinear Spectroscopy of Isotropic Media. I. Third Order. *J. Chem. Phys.* **1996**, *105*, 1.
(61) Tan, H. S.; Piletic, I. R.; Fayer, M. D. Polarization Selective Spectroscopy Experiments: Methodology and Pitfalls. *J. Opt. Soc. Am. B* **2005**, *22*, 2009−2017.
(62) Tao, T. Time-Dependent Fluorescence Depolarization and Brownian Rotational Diffusion Coefficients of Macromolecules. *Biopolymers* **1969**, *8*, 609−632.
(63) Nishida, J.; Fayer, M. D. Theory of Third-Order Spectroscopic Methods to Extract Detailed Molecular Orientational Dynamics for Planar Surfaces and other Uniaxial Systems. *J. Chem. Phys.* **2014**, *140*, 144702.
(64) Moilanen, D. E.; Fenn, E. E.; Lin, Y.-S.; Skinner, J. L.; Bagchi, B.; Fayer, M. D. Water Inertial Reorientation: Hydrogen Bond Strength and the Angular Potential. *Proc. Natl. Acad. Sci. U. S. A.* **2008**, *105*, 5295−5300.
(65) Nishida, J.; Tamimi, A.; Fei, H.; Pullen, S.; Ott, S.; Cohen, S. M.; Fayer, M. D. Structural Dynamics Inside a Functionalized Metal−Organic Framework Probed by Ultrafast 2D IR Spectroscopy. *Proc. Natl. Acad. Sci. U. S. A.* **2014**, *111*, 18442−18447.
(66) Yuan, R.; Yan, C.; Tamimi, A.; Fayer, M. D. Molecular Anion Hydrogen Bonding Dynamics in Aqueous Solution. *J. Phys. Chem. B* **2015**, *119*, 13407−13415.
(67) Bolis, V.; Fubini, B.; Marchese, L.; Martra, G.; Costa, D. Hydrophilic and Hydrophobic Sites on Dehydrated Crystalline and Amorphous Silicas. *J. Chem. Soc., Faraday Trans.* **1991**, *87*, 497−505.
(68) Zhuravlev, L. T. The Surface Chemistry of Amorphous Silica. Zhuravlev Model. *Colloids Surf., A* **2000**, *173*, 1−38.
(69) Kramer, P. L.; Giammanco, C. H.; Fayer, M. D. Dynamics of Water, Methanol, and Ethanol in a Room Temperature Ionic Liquid. *J. Chem. Phys.* **2015**, *142*, 212408.
(70) Rezus, Y. L. A.; Bakker, H. J. On the Orientational Relaxation of HDO in Liquid Water. *J. Chem. Phys.* **2005**, *123*, 114502.
(71) Yuan, R.; Yan, C.; Fayer, M. Ion−Molecule Complex Dissociation and Formation Dynamics in LiCl Aqueous Solutions from 2D IR Spectroscopy. *J. Phys. Chem. B* **2018**, *122*, 10582−10592.
(72) Hoffman, D. J.; Fica-Contreras, S. M.; Pan, J.; Fayer, M. D. Pulse-Shaped Chopping: Eliminating and Characterizing Heat Effects in Ultrafast Infrared Spectroscopy. *J. Chem. Phys.* **2020**, *153*, 204201.
(73) Kinosita, K., Jr.; Kawato, S.; Ikegami, A. A Theory of Fluorescence Polarization Decay in Membranes. *Biophys. J.* **1977**, *20*, 289−305.

https://doi.org/10.1021/acs.jpcb.1c04798
J. Phys. Chem. B 2021, 125, 10018−10034

(74) Lipari, G.; Szabo, A. Effect of Librational Motion on Fluorescence Depolarization and Nuclear Magnetic Resonance Relaxation in Macromolecules and Membranes. *Biophys. J.* **1980**, *30*, 489−506.
(75) Lipari, G.; Szabo, A. Model-Free Approach to the Interpretation of Nuclear Magnetic Resonance Relaxation in Macromolecules. 1. Theory and Range of Validity. *J. Am. Chem. Soc.* **1982**, *104*, 4546−4559.
(76) Debye, P., *Polar Molecules*. Dover: New York, 1929.
(77) Tan, H. S.; Piletic, I. R.; Fayer, M. D. Orientational Dynamics of Water Confined on a Nanometer Length Scale in Reverse Micelles. *J. Chem. Phys.* **2005**, *122*, 174501.
(78) Tamimi, A.; Fayer, M. D. Ionic Liquid Dynamics Measured with 2D IR and IR Pump−Probe Experiments on a Linear Anion and the Influence of Potassium Cations. *J. Phys. Chem. B* **2016**, *120*, 5842−5854.
(79) Kramer, P. L.; Nishida, J.; Giammanco, C. H.; Tamimi, A.; Fayer, M. D. Observation and Theory of Reorientation-Induced Spectral Diffusion in Polarization-Selective 2D IR Spectroscopy. *J. Chem. Phys.* **2015**, *142*, 184505.
(80) Kramer, P. L.; Nishida, J.; Fayer, M. D. Separation of Experimental 2D IR Frequency-Frequency Correlation Functions into Structural and Reorientation-Induced Contributions. *J. Chem. Phys.* **2015**, *143*, 124505.
(81) Giammanco, C. H.; Kramer, P. L.; Yamada, S. A.; Nishida, J.; Tamimi, A.; Fayer, M. D. Carbon Dioxide in an Ionic Liquid: Structural and Rotational Dynamics. *J. Chem. Phys.* **2016**, *144*, 104506.
(82) Tamimi, A.; Bailey, H. E.; Fayer, M. D. Alkyl Chain Length Dependence of the Dynamics and Structure in the Ionic Regions of Room-Temperature Ionic Liquids. *J. Phys. Chem. B* **2016**, *120*, 7488−7501.
(83) Yamada, S. A.; Bailey, H. E.; Tamimi, A.; Li, C.; Fayer, M. D. Dynamics in a Room-Temperature Ionic Liquid from the Cation Perspective: 2D IR Vibrational Echo Spectroscopy. *J. Am. Chem. Soc.* **2017**, *139*, 2408−2420.
(84) Asbury, J. B.; Steinel, T.; Kwak, K.; Corcelli, S. A.; Lawrence, C. P.; Skinner, J. L.; Fayer, M. D. Dynamics of Water Probed with Vibrational Echo Correlation Spectroscopy. *J. Chem. Phys.* **2004**, *121*, 12431−12446.
(85) Asbury, J. B.; Steinel, T.; Stromberg, C.; Corcelli, S. A.; Lawrence, C. P.; Skinner, J. L.; Fayer, M. D. Water Dynamics: Vibrational Echo Correlation Spectroscopy and Comparison to Molecular Dynamics Simulations. *J. Phys. Chem. A* **2004**, *108*, 1107−1119.
(86) Ding, F.; Hu, Z.; Zhong, Q.; Manfred, K.; Gattass, R. R.; Brindza, M. R.; Fourkas, J. T.; Walker, R. A.; Weeks, J. D. Interfacial Organization of Acetonitrile: Simulation and Experiment. *J. Phys. Chem. C* **2010**, *114*, 17651−17659.
(87) Connolly, M. L. Computation of Molecular Volume. *J. Am. Chem. Soc.* **1985**, *107*, 1118−1124.
(88) Romero, C.; Baldelli, S. Sum Frequency Generation Study of the Room-Temperature Ionic Liquids/Quartz Interface. *J. Phys. Chem. B* **2006**, *110*, 6213−6223.
(89) Liu, D.; Ma, G.; Allen, H. C. Adsorption of 4-Picoline and Piperidine to the Hydrated SiO_2 Surface: Probing the Surface Acidity with Vibrational Sum Frequency Generation Spectroscopy. *Environ. Sci. Technol.* **2005**, *39*, 2025−2032.
(90) Zhao, X. S.; Lu, G. Q.; Whittaker, A. K.; Millar, G. J.; Zhu, H. Y. Comprehensive Study of Surface Chemistry of MCM-41 Using ^{29}Si CP/MAS NMR, FTIR, Pyridine-TPD, and TGA. *J. Phys. Chem. B* **1997**, *101*, 6525−6531.
(91) Akaike, H. A New Look at the Statistical Model Identification. *IEEE Trans. Autom. Control* **1974**, *19*, 716−723.
(92) Greenwood, N. N.; Little, R.; Sprague, M. J. The Tellurocyanate Ion, $TeCN^-$. *J. Chem. Soc.* **1964**, 1292−1295.
(93) Kenkre, V. M.; Tokmakoff, A.; Fayer, M. D. Theory of Vibrational Relaxation of Polyatomic Molecules in Liquids. *J. Chem. Phys.* **1994**, *101*, 10618−10629.
(94) Lenchenkov, V.; She, C.; Lian, T. Vibrational Relaxation of CN Stretch of Pseudo-Halide Anions (OCN^-, SCN^-, and $SeCN^-$) in Polar Solvents. *J. Phys. Chem. B* **2006**, *110*, 19990−19997.
(95) Li, S.; Shepherd, T. D.; Thompson, W. H. Simulations of the Vibrational Relaxation of a Model Diatomic Molecule in a Nanoconfined Polar Solvent. *J. Phys. Chem. A* **2004**, *108*, 7347−7355.

https://doi.org/10.1021/acs.jpcb.1c04798
J. Phys. Chem. B 2021, 125, 10018−10034